HAL
open science

Flow-induced vibrations of a rotating cylinder

Rémi Bourguet, David Lo Jacono

To cite this version:

Rémi Bourguet, David Lo Jacono. Flow-induced vibrations of a rotating cylinder. Journal of Fluid Mechanics, 2014, vol. 740, pp. 342-380. 10.1017/jfm.2013.665 . hal-00947888

HAL Id: hal-00947888

https://hal.science/hal-00947888v1

Submitted on 17 Feb 2014

HAL is a multi-disciplinary open access archive for the deposit and dissemination of scientific research documents, whether they are published or not. The documents may come from teaching and research institutions in France or abroad, or from public or private research centers.

L'archive ouverte pluridisciplinaire **HAL**, est destinée au dépôt et à la diffusion de documents scientifiques de niveau recherche, publiés ou non, émanant des établissements d'enseignement et de recherche français ou étrangers, des laboratoires publics ou privés.

Open Archive TOULOUSE Archive Ouverte

(OATAO)

OATAO is an open access repository that collects the work of Toulouse researchers and makes it freely available over the web where possible.

This is an author-deposited version published in : http://oatao.univ-toulouse.fr/
Eprints ID : 10901

To link to this article : DOI:10.1017/jfm.2013.665
URL : http://dx.doi.org/10.1017/jfm.2013.665

To cite this version : Bourguet, Rémi and Lo Jacono, David *Flow-induced vibrations of a rotating cylinder.* (2014) Journal of Fluid Mechanics, vol. 740 . pp. 342-380. ISSN 0022-1120

Any correspondance concerning this service should be sent to the repository administrator: staff-oatao@listes-diff.inp-toulouse.fr

Flow-induced vibrations of a rotating cylinder

Rémi Bourguet† and David Lo Jacono

Institut de Mécanique des Fluides de Toulouse, CNRS, UPS and Université de Toulouse,
31400 Toulouse, France

The flow-induced vibrations of a circular cylinder, free to oscillate in the cross-flow direction and subjected to a forced rotation about its axis, are analysed by means of two- and three-dimensional numerical simulations. The impact of the symmetry breaking caused by the forced rotation on the vortex-induced vibration (VIV) mechanisms is investigated for a Reynolds number equal to 100, based on the cylinder diameter and inflow velocity. The cylinder is found to oscillate freely up to a rotation rate (ratio between the cylinder surface and inflow velocities) close to 4. Under forced rotation, the vibration amplitude exhibits a bell-shaped evolution as a function of the reduced velocity (inverse of the oscillator natural frequency) and reaches 1.9 diameters, i.e. three times the maximum amplitude in the non-rotating case. The free vibrations of the rotating cylinder occur under a condition of wake–body synchronization similar to the lock-in condition driving non-rotating cylinder VIV. The largest vibration amplitudes are associated with a novel asymmetric wake pattern composed of a triplet of vortices and a single vortex shed per cycle, the $T+S$ pattern. In the low-frequency vibration regime, the flow exhibits another new topology, the U pattern, characterized by a transverse undulation of the spanwise vorticity layers without vortex detachment; consequently, free oscillations of the rotating cylinder may also develop in the absence of vortex shedding. The symmetry breaking due to the rotation is shown to directly impact the selection of the higher harmonics appearing in the fluid force spectra. The rotation also influences the mechanism of phasing between the force and the structural response.

Key words: flow–structure interactions, vortex streets, wakes

1. Introduction

Flow-induced vibrations (FIV) of flexible or flexibly mounted bodies with bluff cross-section are encountered in a great variety of physical systems, from the oscillations of plants in wind to the vibrations of risers and mooring lines immersed in ocean currents. Such vibrations cause increased fatigue damage and sometimes failure of the structures. Their modelling, prediction and the elaboration of vibration reduction techniques require a detailed understanding of the underlying fluid–structure interaction mechanisms. The impact of FIV in several civil, wind, offshore and nuclear engineering applications has motivated a number of studies, as collected in Blevins (1990), Naudascher & Rockwell (1994) and Païdoussis, Price & de Langre (2010).

†Email address for correspondence: bourguet@imft.fr

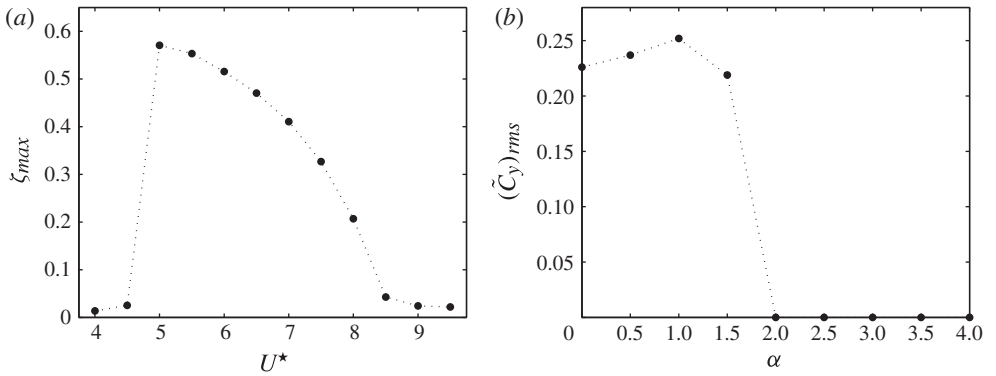

FIGURE 1. (*a*) Maximum amplitude of vibration for a flexibly mounted non-rotating cylinder ($\alpha = 0$) as a function of the reduced velocity. (*b*) The r.m.s. value of the cross-flow force coefficient fluctuation for a rigidly mounted rotating cylinder as a function of the rotation rate.

Vortex formation downstream of a bluff structure induces unsteady forces on the body, which can result in structural vibrations. Vortex-induced vibrations (VIV) are a type of FIV that have been extensively investigated through the canonical problem of a rigid circular cylinder forced or free to oscillate within a cross-flow (Bishop & Hassan 1964; Bearman 1984, 2011; Williamson & Roshko 1988; Mittal & Tezduyar 1992; Hover, Techet & Triantafyllou 1998; Carberry, Sheridan & Rockwell 2001; Jeon & Gharib 2001; Sarpkaya 2004; Williamson & Govardhan 2004; Klamo, Leonard & Roshko 2006; Lucor & Triantafyllou 2008; Dahl *et al.* 2010; Navrose & Mittal 2013). The axial symmetry of a circular cylinder allows VIV to be examined independently of other types of FIV, such as galloping, which is associated with aerodynamically unstable cross-sections (Païdoussis *et al.* 2010). The typical cross-flow response of an elastically mounted circular cylinder is illustrated in figure 1(*a*), where the maximum amplitude of vibration, normalized by the cylinder diameter, is plotted as a function of the reduced velocity, defined as the inverse of the oscillator natural frequency non-dimensionalized by the inflow velocity and the cylinder diameter. Self-excited vibrations appear over a well-defined range of reduced velocities. In this range, the frequency of vortex formation and the frequency of body oscillation coincide; this condition of wake–body synchronization is referred to as lock-in. Under lock-in, the vortex shedding frequency can depart substantially from the Strouhal frequency, i.e. the shedding frequency downstream of a stationary cylinder; also, the vibration frequency can shift considerably away from the natural frequency, owing to changes in the value of the effective added mass (Williamson & Govardhan 2004). The maximum amplitude of VIV responses is generally of the order of one cylinder diameter; it is, however, influenced by structural properties (e.g. mass-damping parameter) and by the Reynolds number (*Re*) (Bearman 2011), and it can reach two diameters at $Re \approx 10^5$ (Raghavan & Bernitsas 2011). In the above-mentioned study and in the present work, the Reynolds number is based on the cylinder diameter and oncoming flow velocity.

VIV can still occur when the symmetry of the body is broken, for instance by considering a square cross-section (Bearman *et al.* 1987; Zhao, Cheng & Zhou 2013). Under broken symmetry, flexibly mounted bodies may also be subjected to the phenomenon of galloping, which is an aerodynamic instability characterized by low-frequency oscillations that increase in amplitude unboundedly with the reduced

velocity (Païdoussis *et al.* 2010). Galloping is driven by the instantaneous angle of attack between the body and the flow, which results in an asymmetric pressure distribution. It does not involve a mechanism of lock-in between the oscillation and vortex formation as opposed to VIV and can thus often be predicted through quasi-steady theory. However, depending on the structure properties, VIV and galloping regions may sometimes overlap (Bearman *et al.* 1987; Corless & Parkinson 1988); the interaction between these two types of FIV leads to intermediate vibration regimes with larger-amplitude responses (Nemes *et al.* 2012).

In the present study, symmetry breaking is introduced through body actuation, by applying a forced rotation to the flexibly mounted circular cylinder. Such configurations may occur in practical applications, as for instance in offshore engineering where drilling risers without casing may be exposed to ocean currents. The possible enhancement of the cylinder free oscillations by the forced rotation may also have implications in the domain of flow energy harvesting. Since the early work of Prandtl (1926), the case of a rigidly mounted circular cylinder subjected to forced rotation within a cross-flow has been the object of many studies, partly due to its potential applications to wake control (e.g. Modi 1997). Different flow regimes have been identified depending on the rotation rate α, defined as the ratio between the cylinder surface velocity and the oncoming flow velocity. Over a wide range of Reynolds numbers, previous experimental and numerical work has shown that the alternate vortex shedding associated with the von Kármán instability vanishes above a rotation rate $\alpha \approx 2$ (Coutanceau & Ménard 1985; Badr *et al.* 1990; Chew, Cheng & Luo 1995; Kang, Choi & Lee 1999; Stojković, Breuer & Durst 2002; Mittal & Kumar 2003; Pralits, Brandt & Giannetti 2010). A secondary region of unsteady wake where one-sided vortices form at much lower frequency has been reported over a small range of rotation rates, for $\alpha > 4$ (Mittal & Kumar 2003; Stojković *et al.* 2003; Pralits *et al.* 2010). The imposed rotation alters the flow three-dimensional transition. Through direct numerical simulation and stability analysis, El Akoury *et al.* (2008) and Rao *et al.* (2013*b*) have shown that the rotation increases the critical Reynolds number of the secondary instability associated with the spanwise undulation of the von Kármán vortices. The three-dimensional transition scenario involves wake modes similar to those identified in the non-rotating cylinder case (i.e. modes A and B (Williamson 1988)) but also new steady and unsteady modes, depending on the rotation rate and Reynolds number (Rao *et al.* 2013*b*). Over a range of high rotation rates, Mittal (2004) and Meena *et al.* (2011) presented evidence that the three-dimensional transition may occur through flow patterns comparable to those observed due to centrifugal instabilities in flows between two concentric rotating cylinders. They showed that such three-dimensional patterns appear in both steady and unsteady flow regimes. On the basis of linear stability analyses, Pralits, Giannetti & Brandt (2013) and Rao *et al.* (2013*a*) recently emphasized that the imposed rotation may cause three-dimensional transition down to $Re \approx 30$; at $Re = 100$, they reported a critical rotation rate close to 3.7.

The passage from unsteady to steady flow at $\alpha \approx 2$ is accompanied by the suppression of the fluid force fluctuations, as illustrated in figure 1(*b*), where the root mean square (r.m.s.) value of the cross-flow force coefficient fluctuation exerted on a rigidly mounted rotating cylinder is plotted as a function of the rotation rate. The question arises whether the structural vibrations will be cancelled by the rotation in this range of α once the cylinder is free to oscillate.

The problem of a flexibly mounted circular cylinder with imposed rotation in a cross-current has received much less attention than the rigidly mounted body case.

Through experiments and numerical simulations, Stansby & Rainey (2001) examined the case of a rotating circular cylinder free to vibrate in both the in-line and cross-flow directions, in the Reynolds number range 200–4700. For $\alpha \in [2, 5]$ and depending on the reduced velocity, they reported large oscillations of the cylinder, with peak amplitudes higher than 10 diameters. These low-frequency galloping-like responses occur without lock-in; instead, vortex formation leads to high-frequency oscillations of the force coefficients that are superimposed on the low-frequency oscillations associated with the cylinder responses. Yogeswaran & Mittal (2011) confirmed these observations at $\alpha = 4.5$ and $Re = 200$, and provided flow visualizations emphasizing the absence of synchronization between the cylinder large-amplitude low-frequency oscillations and the vortex formation. Previous work has focused on two-degree-of-freedom oscillators, which have been shown to be prone to galloping responses when the cylinder is subjected to forced rotation. Hence, the behaviour of the system is under question when the rotating cylinder is free to oscillate only in the cross-flow direction. In addition, previous studies did not analyse the effect of the rotation in the regime where wake and body oscillations are synchronized; the influence of forced rotation on VIV phenomenon remains to be elucidated. The possible consequences, on the cylinder responses, of the flow three-dimensional transition at high rotation rates also need to be clarified. These aspects are addressed in the present work.

The impact of symmetry breaking, through imposed rotation of the cylinder, on the fluid–structure interaction mechanisms previously examined in the non-rotating case is investigated in this study by means of a joint analysis of the body responses, wake patterns and fluid forces. A flexibly mounted circular cylinder, free to oscillate in the cross-flow direction, is considered over a wide range of reduced velocities and rotation rates. The range of rotation rates includes the transition region where vortex shedding is suppressed by the rotation in the rigidly mounted body case. The Reynolds number is chosen equal to 100, which ensures a two-dimensional flow over most of the parameter space, except in the range of high rotation rates. The parametric study is based on two- and three-dimensional numerical simulations of the flow past a flexibly mounted body.

The paper is organized as follows. The physical fluid–structure model and the numerical method are presented in § 2. The cylinder responses are quantified in § 3. The flow patterns encountered in the wake of the flexibly mounted rotating cylinder are described in § 4. The fluid forces are analysed in § 5. The three-dimensional transition in the flow is examined in § 6. Finally, the main findings of the present work are summarized in § 7.

2. Formulation and numerical method

The physical configuration and its modelling are described in § 2.1. The numerical method employed and its validation are presented in § 2.2.

2.1. *Fluid–structure system*

A sketch of the physical configuration is presented in figure 2. The elastically mounted rigid cylinder has a circular cross-section; it is immersed in a cross-flow that is parallel to the x axis and normal to the cylinder axis (z axis). The Reynolds number based on the oncoming flow velocity (U) and cylinder diameter (D), $Re = \rho_f UD/\mu$, where ρ_f and μ denote the fluid density and viscosity, is set equal to 100. The flow is assumed to be incompressible. At $Re = 100$, the flow remains two-dimensional over most of the parameter space investigated; therefore, the two-dimensional Navier–Stokes equations

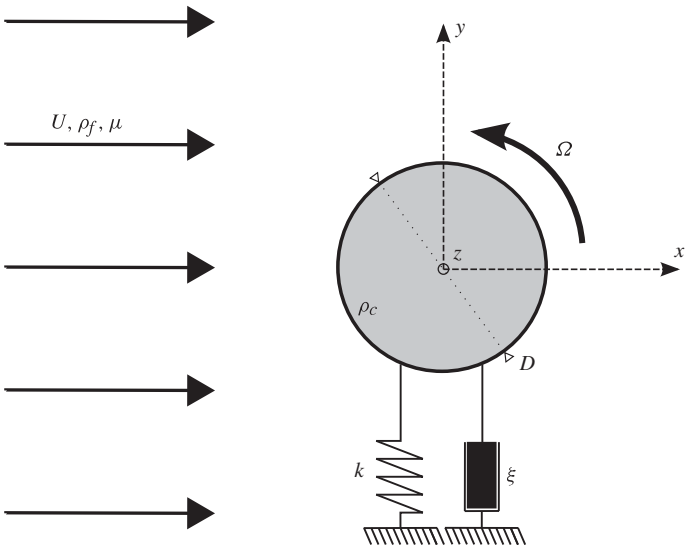

FIGURE 2. Sketch of the physical configuration.

are generally employed to predict the flow dynamics. In order to study the flow three-dimensional transition at high rotation rates, the three-dimensional Navier–Stokes equations are also considered at selected points of the parameter space. In the three-dimensional case, an aspect ratio of $L/D = 10$, where L is the cylinder length in the spanwise direction (z axis), is selected as a reasonable balance between the wavelength of the flow three-dimensional pattern (of the order of (1–2)D) and the numerical cost.

The cylinder is fixed in the in-line direction (x axis) and free to oscillate in the cross-flow direction (y axis). The structure/fluid mass ratio, $m = \rho_c/\rho_f D^2$, where ρ_c is the body mass per unit length, is set to a value of 10. The structural stiffness and damping ratio are designated by k and ξ. In the following, all the physical variables are non-dimensionalized by the cylinder diameter and the oncoming flow velocity. The non-dimensional cylinder displacement, velocity and acceleration are denoted by ζ, $\dot{\zeta}$ and $\ddot{\zeta}$, respectively. The sectional in-line and cross-flow force coefficients are defined as $C_x = 2F_x/\rho_f DU^2$ and $C_y = 2F_y/\rho_f DU^2$, where F_x and F_y are the in-line and cross-flow dimensional sectional fluid forces. The body dynamics is governed by a forced second-order oscillator equation, which can be expressed as follows, in non-dimensional formulation:

$$\ddot{\zeta} + \frac{4\pi\xi}{U^\star}\dot{\zeta} + \left(\frac{2\pi}{U^\star}\right)^2 \zeta = \frac{C_y}{2m}. \tag{2.1}$$

Here $U^\star$ denotes the reduced velocity, $U^\star = 1/f_n$, where f_n is the non-dimensional natural frequency in vacuum, $f_n = D/2\pi U\sqrt{k/\rho_c}$. The structural damping is set equal to zero ($\xi = 0$) to allow maximum-amplitude oscillations. In the three-dimensional flow case, the span-averaged fluid force coefficient is considered in (2.1).

The cylinder is subjected to a forced, anticlockwise, steady rotation about its axis. The imposed rotation is controlled by the rotation rate $\alpha = \Omega D/2U$, where Ω is the angular velocity of the cylinder.

The present parametric study focuses on α and $U^\star$. Previous work concerning rigidly mounted rotating cylinders has shown that the critical value of the rotation rate for

suppression of the vortex shedding at $Re = 100$ is $\alpha \approx 1.8$ (Kang *et al.* 1999; Stojković *et al.* 2003). A range of rotation rates including this transition is considered, namely $\alpha \in \{0, 0.5, 1.0, 1.5, 2.0, 2.5, 3.0, 3.5, 3.75, 4.0\}$. The reduced velocity is varied from 4 to 34 with a step equal to 0.5.

2.2. *Numerical simulation method*

The coupled fluid–structure system is solved by the parallelized code *Nektar*, which is based on the spectral/*hp* element method (Karniadakis & Sherwin 1999). The version of the code employs a Jacobi–Galerkin formulation in the (x, y) plane and a Fourier expansion in the spanwise (z) direction (for three-dimensional simulations). A boundary-fitted coordinate formulation is used to take into account the cylinder displacement. Details concerning the numerical method, including the time integration schemes, and its implementation have been reported in Newman & Karniadakis (1997) and Evangelinos & Karniadakis (1999) for similar configurations.

A non-dimensional time step ranging from 0.001 to 0.005 is selected, depending on the rotation rate. As noted by Mittal & Kumar (2003), the size of the computational domain may substantially impact the simulation results, especially at high rotation rates. To avoid any spurious blockage effects due to domain size, a large rectangular domain is considered in the present simulations: $350D$ downstream; and $250D$ in front, above and below the cylinder. A no-slip condition is applied on the cylinder surface. The free-stream value is assigned for the velocity at the upstream boundary. At the downstream boundary, a Neumann-type boundary condition is used. Flow periodicity conditions are employed on the upper and lower boundaries, as well as on the side (spanwise) boundaries in the three-dimensional case. A two-dimensional grid of 3975 spectral elements is used in the (x, y) plane. The evolutions of the time-averaged force coefficients as functions of the spectral element polynomial order, for a rigidly mounted cylinder at $\alpha = 4$ (the largest rotation rate considered in this paper) and for a flexibly mounted cylinder at $(\alpha, U^\star) = (3.75, 13)$ (i.e. in the region of maximum vibration amplitude, as shown in § 3), are plotted in figure 3. In the former case, the rotation cancels the vortex shedding and the flow is steady, thus $\overline{C}_x = C_x$ and $\overline{C}_y = C_y$, where the over-bar denotes time-averaged values. It can be observed that an increase from order four to five has no significant influence on the results; hence, a polynomial order equal to four is selected. For the three-dimensional simulations, 64 complex Fourier modes (i.e. 128 planes) are employed in the spanwise direction.

The simulation approach is validated by comparison with previous results reported in the literature concerning a stationary cylinder (table 1), a flexibly mounted non-rotating cylinder (table 2) and a rigidly mounted rotating cylinder (figure 4). In the three cases, the present results are in good agreement with previous work, which ensures the validity of the parametric study reported in this paper.

All the simulations are initialized with the established periodic flow past a stationary cylinder at $Re = 100$; then the forced rotation is started and the cylinder is released. The analysis is based on time series of more than 40 oscillation cycles (or vortex shedding cycles in the absence of vibrations), collected after the initial transient dies out. Convergence of each simulation is established by monitoring the time-averaged and r.m.s. values of the fluid force coefficients and body displacement.

3. Structural responses

The responses of the flexibly mounted cylinder subjected to forced rotation are quantified in this section. For periodic oscillations and forces, as those typically

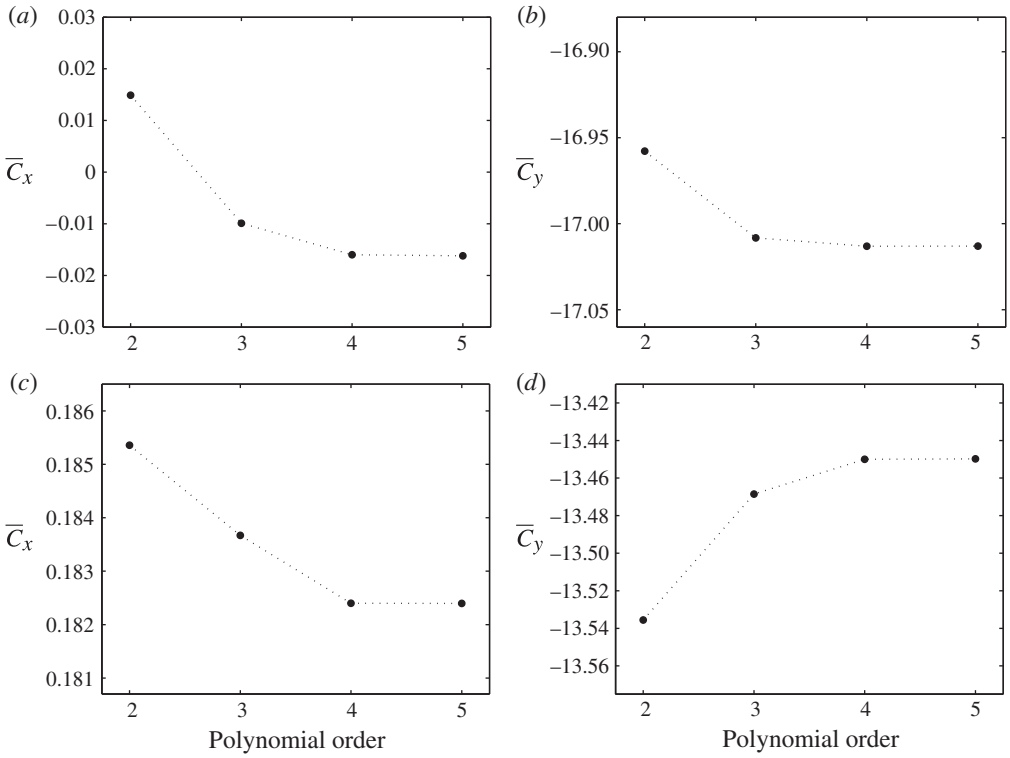

FIGURE 3. Time-averaged (*a*,*c*) in-line and (*b*,*d*) cross-flow force coefficients as functions of the polynomial order, for (*a*,*b*) a rigidly mounted rotating cylinder at $\alpha = 4$ and (*c*,*d*) a flexibly mounted rotating cylinder at $(\alpha, U^{\star}) = (3.75, 13)$ at $Re = 100$.

Study	St	$\overline{C}_x$	$(C_y)_{max}$
Braza, Chassaing & Ha Minh (1986)	0.16	1.28	0.29
Stansby & Slaouti (1993)	0.166	1.32	0.35
Kang *et al.* (1999)	0.165	1.32	0.32
Zhou, So & Lam (1999)	0.162	1.48	0.31
Kim, Kim & Choi (2001)	0.165	1.33	0.32
Shiels, Leonard & Roshko (2001)	0.167	1.33	0.30
Stojković *et al.* (2002)	0.165	1.34	0.33
Shen, Chan & Lin (2009)	0.166	1.38	0.33
Present	0.164	1.32	0.32

TABLE 1. Strouhal number, time-averaged in-line force coefficient and maximum cross-flow force coefficient for a stationary cylinder (i.e. rigidly mounted and non-rotating), at $Re = 100$, from previous work and the current paper.

observed in this work, the time-averaged displacement of the cylinder can be expressed as $\overline{\zeta} = U^{\star 2}\overline{C}_y/8\pi^2 m$ by considering the time-averaged form of the structure dynamics (2.1). As shown in figure 4(*b*), where the time-averaged cross-flow force coefficient is plotted as a function of the rotation rate in the rigidly mounted cylinder

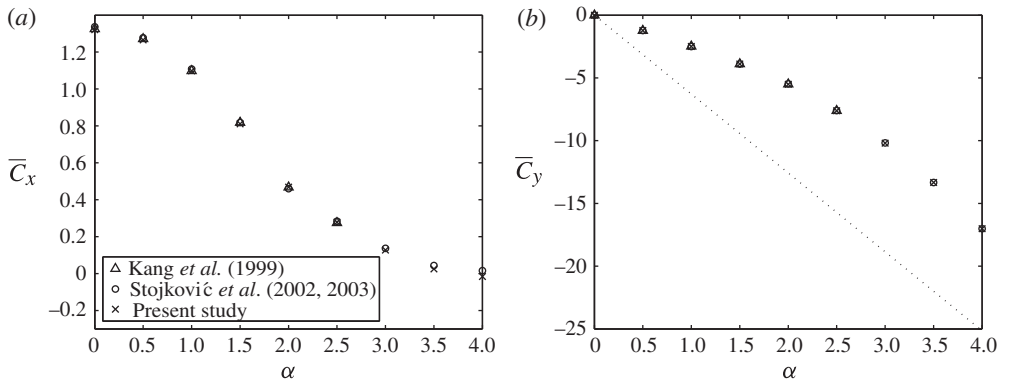

FIGURE 4. Time-averaged (*a*) in-line and (*b*) cross-flow force coefficients for a rigidly mounted rotating cylinder as functions of the rotation rate, at $Re = 100$. In panel (*b*) the dotted line indicates the cross-flow force coefficient in the potential flow case.

Study	$(\zeta)_{max}$	f	$\overline{C}_x$	$(C_y)_{max}$
Shiels *et al.* (2001)	0.58	0.196	2.22	0.77
Shen *et al.* (2009)	0.57	0.190	2.15	0.83
Present	0.57	0.188	2.08	0.88

TABLE 2. Maximum amplitude of vibration, vibration frequency, time-averaged in-line force coefficient and maximum cross-flow force coefficient for a flexibly mounted non-rotating ($\alpha = 0$) cylinder at $Re = 100$, for $m = 1.25$, $\xi = 0$ and $U^\star = 4.46$, from previous work and the current paper.

case, the magnitude of $\overline{C}_y$ increases with α (Magnus effect (Prandtl 1926)); the negative sign is due to the anticlockwise rotation. As also noted in previous studies (e.g. Mittal & Kumar 2003), $\overline{C}_y$ differs substantially from the prediction through potential flow theory ($C_y = -2\pi\alpha$; dotted line), and exceeds the limit of 4π proposed by Prandtl (1926). A similar trend of $\overline{C}_y$ versus α is noted in the flexibly mounted cylinder case, as shown in § 5. As a consequence, for a given reduced velocity, a global decrease of $\overline{\zeta}$ is expected as α increases. This behaviour is verified in figure 5, where the time-averaged displacement of the body is plotted as a function of the reduced velocity, for each rotation rate. The actual responses of the flexibly mounted cylinder follow the trends obtained by considering the above time-averaged form of the dynamics equation and the mean force coefficients issued from the rigidly mounted body case (dashed lines). Some differences can be noted, as for instance for $\alpha = 3.75$ around $U^\star = 14$; this highlights the alteration of the time-averaged forces under body vibrations, which is discussed in § 5.

The maximum amplitude of the cylinder oscillation about its time-averaged position ($\tilde{\zeta}$) is plotted as a function of the rotation rate and reduced velocity in figure 6(*a*,*b*). The cylinder exhibits large-amplitude vibrations over a wide zone of the parameter space. As a general trend, it appears that the response peak amplitude and the width of the $U^\star$ range where large-amplitude oscillations occur first increase with α and then drop abruptly. For a better visualization of the vibration region in the (α, $U^\star$)

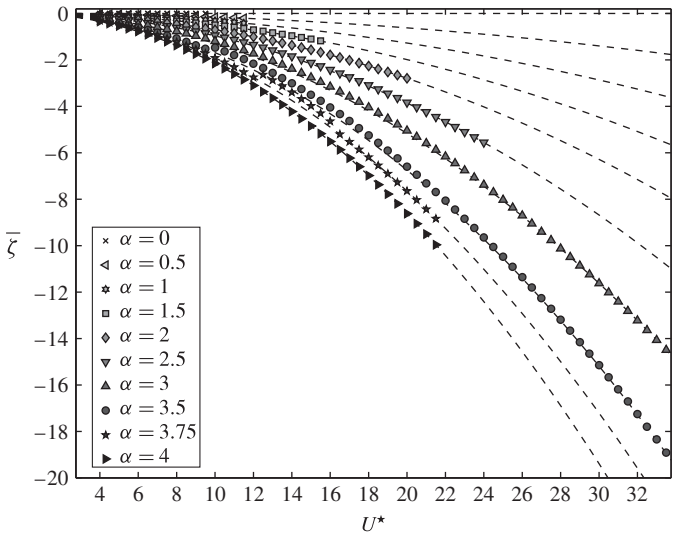

FIGURE 5. Time-averaged displacement as a function of the reduced velocity. For each rotation rate, a dashed line indicates the displacement induced by the time-averaged cross-flow force issued from the rigidly mounted cylinder case, as plotted in figure 4(*b*).

domain, the area where oscillations larger than $0.05D$ are observed is represented by the hatched zone in figure 6(*c*). Vibrations are noted for $\alpha < 1.8$, in a region where the flow past a rigidly mounted cylinder is unsteady, but also for $\alpha \geqslant 1.8$, where the rotation suppresses the vortex formation in the rigidly mounted body case (e.g. Kang *et al.* 1999; Stojković *et al.* 2002). No vibration is observed for $\alpha = 4$.

As shown in figure 7(*a*), where the maximum amplitude of oscillation is plotted as a function of $U^\star$, the cylinder may reach vibration amplitudes close to $1.9D$ under forced rotation, i.e. more than three times larger than the peak amplitude in the non-rotating case. A drift of the peak amplitude towards higher values of $U^\star$ can be noted as α increases, for $\alpha \leqslant 3$; the trend reverses for larger values of α. The present vibrations exhibit lower amplitudes than the galloping-like responses reported by Stansby & Rainey (2001) and Yogeswaran & Mittal (2011) for a rotating cylinder free to oscillate in both the in-line and cross-flow directions. The amplitude of galloping vibrations increases continuously with $U^\star$. Instead, the response amplitudes of the present rotating cylinder exhibit bell-shaped evolutions as functions of the reduced velocity, which resemble the typical VIV behaviour of the non-rotating case ($\alpha = 0$). This suggests that, like VIV, the vibrations of the present rotating cylinder may occur under a wake–body synchronization mechanism, as opposed to galloping vibrations, which do not involve such synchronization. This aspect is clarified in the following sections.

The oscillations of the rotating cylinder are generally periodic and exhibit a strong sinusoidal nature. The spectral amplitudes of the higher harmonics that may appear in the response always remain below 5 % of the first harmonic amplitude. The vibration frequency normalized by the natural frequency in vacuum ($f^\star = f/f_n$, with f the non-dimensional vibration frequency) is plotted as a function of the reduced velocity in figure 7(*b*). The overall evolution of the response frequency in the rotating cylinder cases is comparable to the VIV behaviour observed at $\alpha = 0$. In the range of low

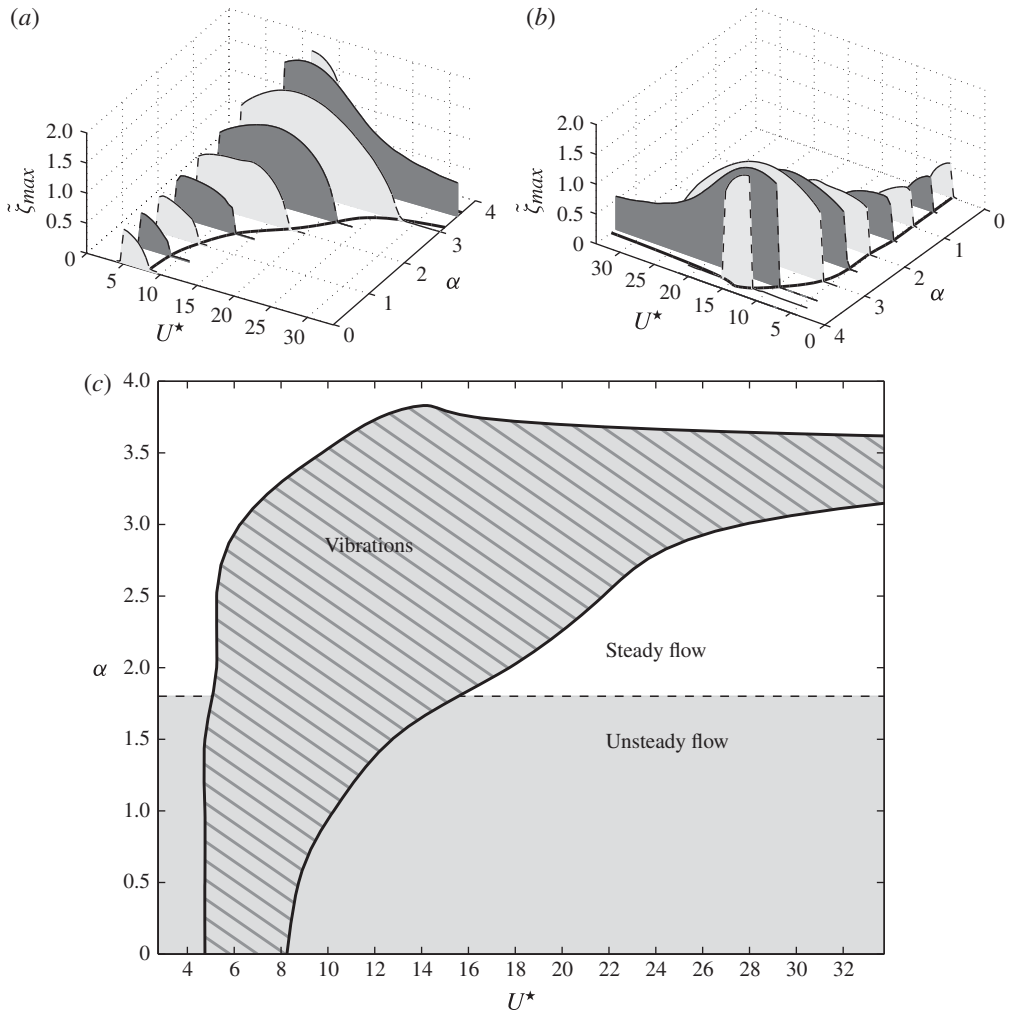

FIGURE 6. (*a*,*b*) Maximum amplitude of vibration as a function of the rotation rate and reduced velocity. (*c*) Region of vibration (hatched area) in the rotation rate–reduced velocity domain. The limit of the vibration region is indicated by the plain black line. In panel (*c*), the dashed line represents the limit between the steady and unsteady flow regimes, outside the vibration region.

reduced velocities, the vibration frequency bends downwards to follow approximately the normalized vortex shedding frequency observed in the stationary cylinder case (dashed line; Strouhal number in the range 0.163–0.165 in the rotating cases, thus close to the non-rotating case value). At higher values of $U^\star$, the response frequency remains relatively constant, but generally differs from the natural frequency ($f^\star \neq 1$). The initial bending towards the Strouhal frequency, observed at low values of $U^\star$, also appears for rotation rates associated with a suppression of the vortex shedding in the rigidly mounted cylinder case. A global decrease of the vibration frequency can be noted as α increases; this phenomenon will be connected to the variability of the effective added mass in § 5.

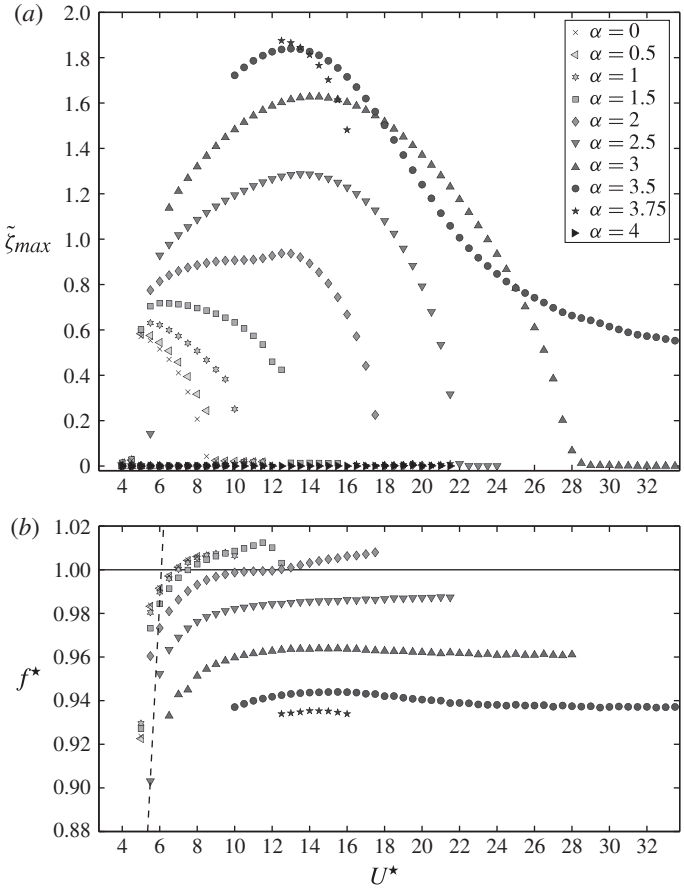

FIGURE 7. (*a*) Maximum amplitude of vibration and (*b*) normalized vibration frequency as functions of the reduced velocity. In panel (*b*), the dashed line indicates the normalized frequency of vortex shedding in the stationary cylinder case.

The flow patterns occurring in the wake of the freely vibrating rotating cylinder are examined in the next section.

4. Wake patterns

The vortex shedding patterns encountered downstream of a non-rotating cylinder subjected to forced or free vibrations have been identified and classified in previous studies (Williamson & Roshko 1988; Brika & Laneville 1993; Govardhan & Williamson 2000; Carberry, Sheridan & Rockwell 2005). These works have shown that the flow patterns may differ substantially from the alternate shedding observed in the stationary cylinder case. Similarly, the impact of forced rotation on the wake of a rigidly mounted cylinder has been extensively analysed (Badr *et al.* 1990; Stojković *et al.* 2002; Mittal & Kumar 2003; Pralits *et al.* 2010). The question that arises is whether similar patterns will appear in the flow when the cylinder is subjected to free vibrations under forced rotation. This question is addressed in this section, and particular attention is paid to the possible occurrence of new wake patterns.

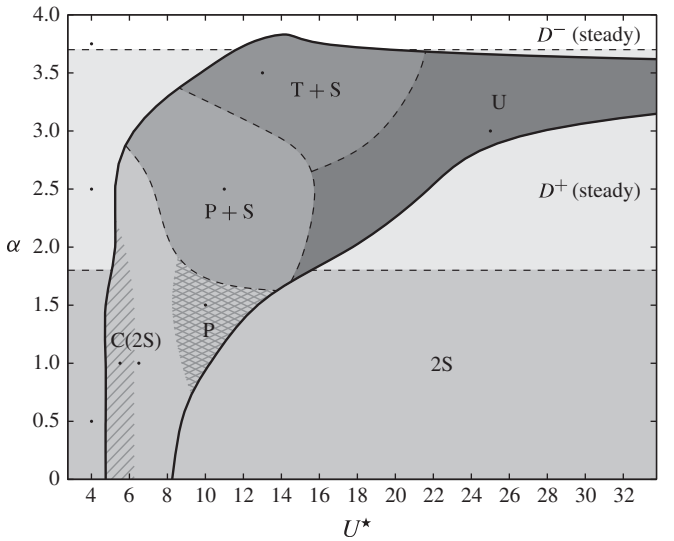

FIGURE 8. Wake pattern as a function of the rotation rate and reduced velocity. The limit of the vibration region is indicated by the plain black line. The black dots denote the cases considered in figures 9–11.

A map of the different wake patterns in the $(\alpha, U^\star)$ domain is presented in figure 8. The map is based on two-dimensional flow simulation results. The three-dimensional transition that occurs at high rotation rates ($\alpha > 3.5$) is investigated in § 6. A number of additional simulations have been performed to locate the limits of the regions associated with each wake pattern. However, it should be mentioned that the limits indicated in figure 8 are approximate, since pattern switching and hysteresis phenomena may appear in the transition zones (Khalak & Williamson 1999; Prasanth & Mittal 2008). The different wake patterns are illustrated in figures 9–11 by instantaneous isocontours of spanwise vorticity, for selected values of the pair $(\alpha, U^\star)$, which are designated by black dots in figure 8. In these figures, the cross-flow trajectory of the body centre is indicated by the black segments.

The limit of the vibration region identified in § 3 is denoted by a plain black line in figure 8. Outside the vibration region, the wake patterns are those reported in previous studies concerning rigidly mounted rotating cylinders. At low rotation rates, for $\alpha < 1.8$, the wake exhibits the 2S pattern, which is characterized by two counter-rotating vortices shed per cycle, as in the stationary cylinder case (figure 9*a*). As also noted in previous studies (e.g. Mittal & Kumar 2003), the rotation induces an asymmetry in the strength of the positive and negative vortices, and an upward deviation of the wake. For $\alpha \geqslant 1.8$, the wake is composed of two layers of vorticity of opposite signs and deflected upwards (figure 9*b*,*c*); the flow is steady. At sufficiently high rotation rates, the negative-vorticity tongue wraps around the cylinder and a switch of the two layers of vorticity can be noted in the wake, i.e. the positive-vorticity layer is now located above the negative-vorticity layer (figure 9*c*). In this case, the wake resembles to some extent a jet-like wake. The inversion of the vorticity layers can be related to the change observed in the sign of the in-line force (i.e. drag) at $\alpha \approx 3.7$, as shown in figure 4(*a*). The two steady wake patterns are referred to as D^+ and D^-, in reference to the positive or negative value of the drag. The switch from positive to negative drag is chosen to define the limit between the D^+ and D^- pattern regions.

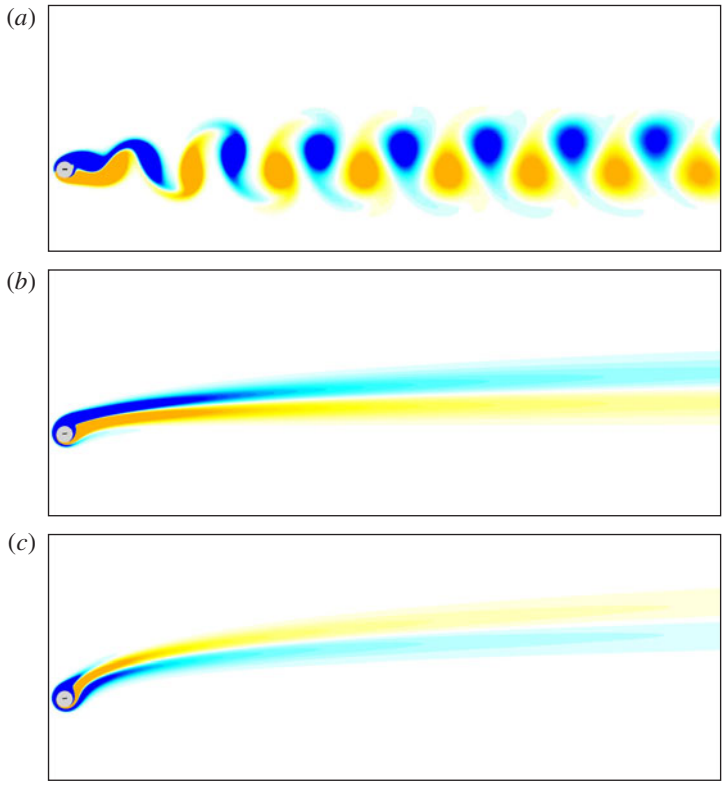

FIGURE 9. (Colour online) Instantaneous isocontours of vorticity: (*a*) 2S pattern, $(\alpha, U^\star) = (0.5, 4)$, $\omega_z = \pm 0.4$; (*b*) D^+ pattern, $(\alpha, U^\star) = (2.5, 4)$, $\omega_z = \pm 0.2$; (*c*) D^- pattern, $(\alpha, U^\star) = (3.75, 4)$, $\omega_z = \pm 0.2$. Positive and negative vorticity values are plotted in pale grey and dark grey (yellow and blue online), respectively. Part of the computational domain is shown.

The evolution of the structural response amplitude as a function of the reduced velocity, presented in § 3 (figure 7*a*), suggested that the vibrations of the rotating cylinder were synchronized with wake oscillations. As shown in § 5 by spectral analysis, this hypothesis is verified: within the vibration region identified in the $(\alpha, U^\star)$ domain, the cylinder response frequency coincides with the predominant frequency of the wake, i.e. the lock-in condition is established.

Within the vibration region, all the wake patterns encountered thus occur under wake–body synchronization. The area of lower rotation rates is characterized by the 2S pattern (figure 10*a*) and variations of the 2S pattern (figure 10*b*,*c*). In the range of low reduced velocities, the vortices tend to coalesce in the wake (figure 10*b*); this pattern, also observed in a similar range of $U^\star$ in previous studies concerning free vibrations of a non-rotating cylinder (e.g. Singh & Mittal 2005), is referred to as C(2S). In the range of high reduced velocities, the two counter-rotating vortices shed during each cycle regroup and form pairs, which resemble the P pattern reported by Williamson & Roshko (1988) for forced vibrations of large amplitude. At higher rotation rates, the region of intermediate reduced velocities is dominated by a mixed pattern composed of a pair (P) of vortices coupled to a single (S) vortex (figure 11*a*). This pattern, referred to as P + S, has previously been observed in the wake of non-rotating cylinders under

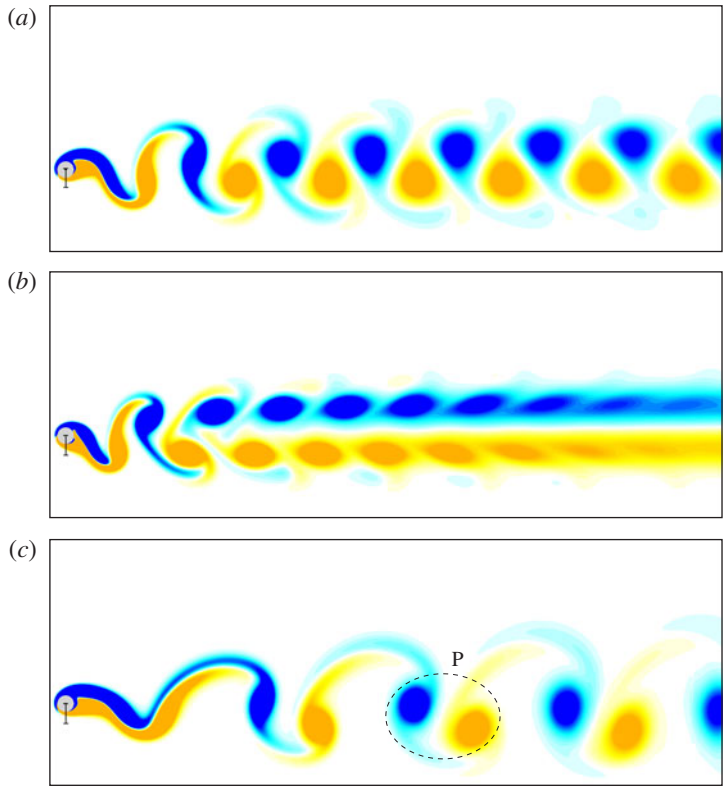

FIGURE 10. (Colour online) Instantaneous isocontours of vorticity: (*a*) 2S pattern, $(\alpha,\ U^{\star}) = (1,\ 6.5)$, $\omega_z = \pm 0.4$; (*b*) C(2S) pattern, $(\alpha,\ U^{\star}) = (1,\ 5.5)$, $\omega_z = \pm 0.4$; (*c*) P pattern, $(\alpha,\ U^{\star}) = (1.5,\ 10)$, $\omega_z = \pm 0.3$. Positive and negative vorticity values are plotted in pale grey and dark grey (yellow and blue online), respectively. Part of the computational domain is shown. The trajectory of the cylinder centre is indicated by the black segment.

forced and free oscillations (Blackburn & Henderson 1999; Singh & Mittal 2005). In the range of intermediate reduced velocities and for $\alpha > 2.5$ approximately, a fourth vortical structure appears during each shedding cycle, as shown in figure 11(*b*). This type of shedding clearly differs from the 2P pattern where two vortex pairs of similar topology are shed per cycle; as an extension of the P + S pattern, this pattern may be referred to as T + S, by regrouping the three vortices into a triplet (T), as indicated in figure 11(*b*). Shedding of two vortex triplets (2T) has been observed for a non-rotating cylinder subjected to both in-line and cross-flow VIV (e.g. Dahl *et al.* 2007). To the authors' knowledge, the existence of the present T + S pattern has not previously been reported. The last zone of the vibration region, principally associated with high reduced velocities, is dominated by another novel type of wake pattern, which was not documented in the literature on cylinder VIV: the wake is composed of two undulating vorticity layers, without shedding of vortical structures (figure 11*c*). Because of its undulatory nature, this pattern is referred to as U.

Previous studies concerning oscillating non-rotating cylinders have highlighted the influence of the oscillation amplitude and frequency on wake pattern selection (e.g. Williamson & Roshko 1988). In order to examine how the flow topology relates to the vibration characteristics in the present rotating cylinder case, the pattern selected

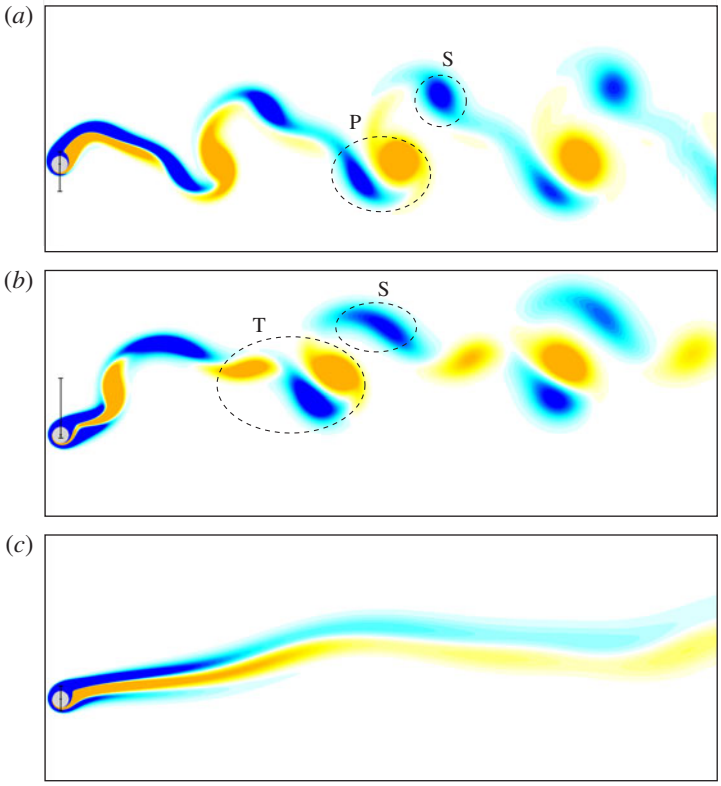

FIGURE 11. (Colour online) Instantaneous isocontours of vorticity: (*a*) P + S pattern, $(\alpha, U^{\star}) = (2.5, 11)$, $\omega_z = \pm 0.2$; (*b*) T + S pattern, $(\alpha, U^{\star}) = (3.5, 13)$, $\omega_z = \pm 0.15$; (*c*) U pattern, $(\alpha, U^{\star}) = (3, 25)$, $\omega_z = \pm 0.1$. Positive and negative vorticity values are plotted in pale grey and dark grey (yellow and blue online), respectively. Part of the computational domain is shown. The trajectory of the cylinder centre is indicated by the black segment.

for each pair $(\alpha, U^{\star})$ is indicated in figure 12 in the response amplitude–frequency domain. Except in a small area in the low-frequency zone ($f \approx 0.05$) where the U and T + S patterns overlap, each wake pattern appears to be associated with a specific region of the $(\tilde{\zeta}_{max}, f)$ domain. The 2S pattern and its variations (C(2S) and P) are mainly related to structural responses of moderate amplitudes and high to moderate frequencies. Similarities may be noted with the map of wake patterns obtained through forced vibration experiments by Williamson & Roshko (1988), in the non-rotating cylinder case: the transition from 2S to C(2S) patterns as the vibration frequency increases, as well as the occurrence of the P + S pattern for $\tilde{\zeta}_{max} > 0.8$ approximately, are in agreement with this previous work. Owing to the imposed rotation, significant differences exist, as for instance the occurrence of the P pattern in the region of low-amplitude responses. The P + S and T + S patterns are associated with large-amplitude vibrations at moderate to low frequencies; the T + S pattern dominates the region of maximum-amplitude vibrations. It can be observed that the U pattern, which dominates the low-frequency zone, appears over a wide range of oscillation amplitudes.

As mentioned above, the vibrations of the rotating cylinder develop under the lock-in condition, which is the key mechanism of VIV. However, the self-sustained

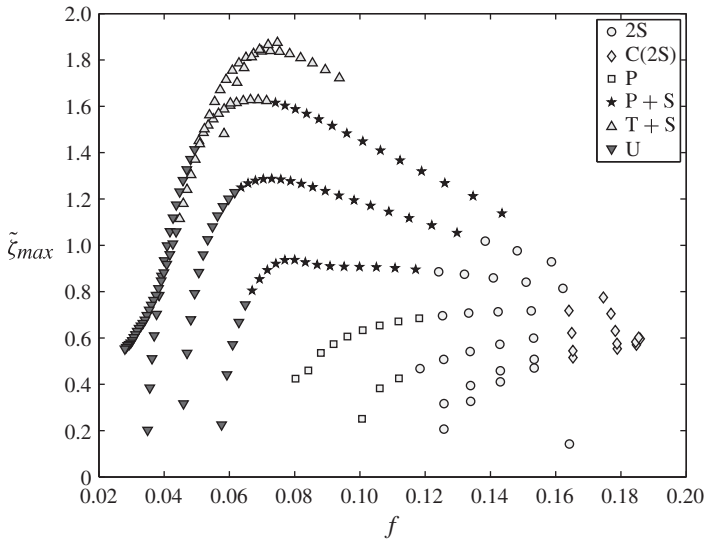

FIGURE 12. Wake pattern as a function of the vibration maximum amplitude and frequency.

oscillations occurring in the region of the U pattern, and thus excited by the flow in the absence of vortex shedding, cannot be rigorously called *vortex-induced* vibrations. Therefore, the more general terminology *flow-induced vibrations under wake–body synchronization* is preferred to designate the responses of the rotating cylinder. This terminology also allows one to distinguish the present fluid–structure interaction phenomenon from galloping, which does not involve the lock-in condition.

The next section focuses on the forces exerted by the flow on the flexibly mounted rotating cylinder.

5. Fluid forces

In order to further investigate the interaction mechanisms, a detailed analysis of the fluid forces is reported in this section. An overview of the typical features of the fluid forces and energy transfer is presented in § 5.1. Systematic statistical and spectral analyses are performed in § 5.2 with an emphasis on the occurrence of higher harmonics in the force spectra. The phasing mechanisms between force and displacement are addressed in § 5.3. The effective added mass induced by the fluid is examined in § 5.4.

5.1. *Temporal evolutions in selected configurations*

Three configurations associated with three points in the $(\alpha, U^\star)$ domain are considered at first to highlight some properties of the fluid forces. Focus is placed on the cross-flow force, since it is the component that drives the cylinder response. A global analysis encompassing the entire parameter space and including the in-line force component is reported in the following subsections. The selected configurations cover a wide range of body oscillation amplitudes and frequencies; they correspond to the 2S (figure 13), T + S (figure 14) and U (figure 15) wake patterns identified in § 4. For each case, time series of the fluctuations of the cross-flow force coefficient ($\tilde{C}_y$) and of the pressure ($\tilde{C}_y^p$) and viscous ($\tilde{C}_y^v$) parts of this force coefficient (figures

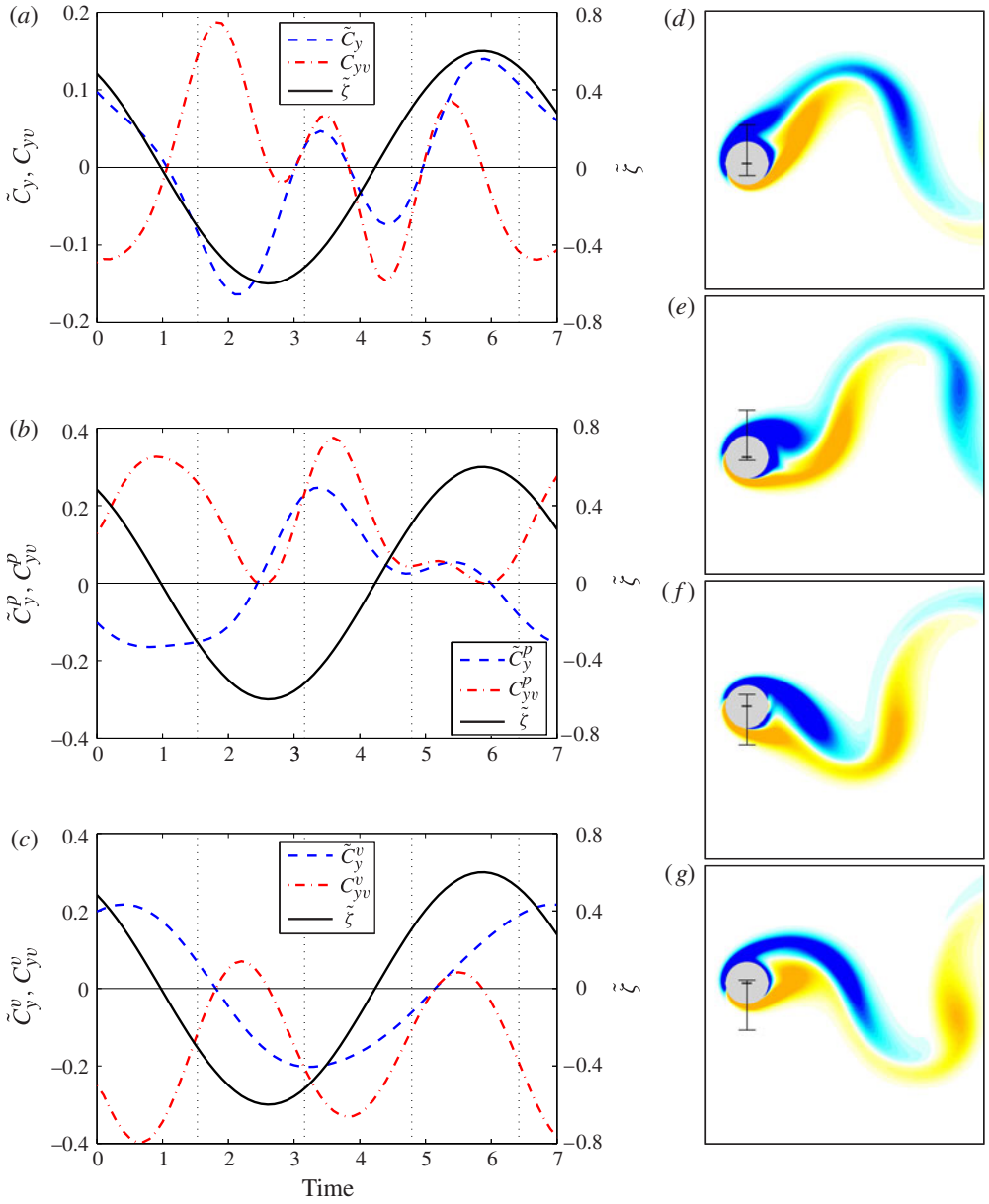

FIGURE 13. (Colour online) (*a–c*) Temporal evolution of the cross-flow force coefficient fluctuation (dashed line; left axis) and cylinder displacement fluctuation (solid line; right axis) for $(\alpha, U^{\star}) = (1, 6.5)$ – 2S pattern: (*a*) total, (*b*) pressure and (*c*) viscous. The instantaneous power due to the corresponding force component is also shown (dash-dotted line; left axis). (*d–g*) Instantaneous isocontours of vorticity at the times indicated by vertical dotted lines in panels (*a–c*). Positive and negative vorticity values are plotted in pale grey and dark grey (yellow and blue online), respectively, in the range $\omega_z = \pm 2.5$. Part of the computational domain is shown. The trajectory of the cylinder centre is indicated by the black segment.

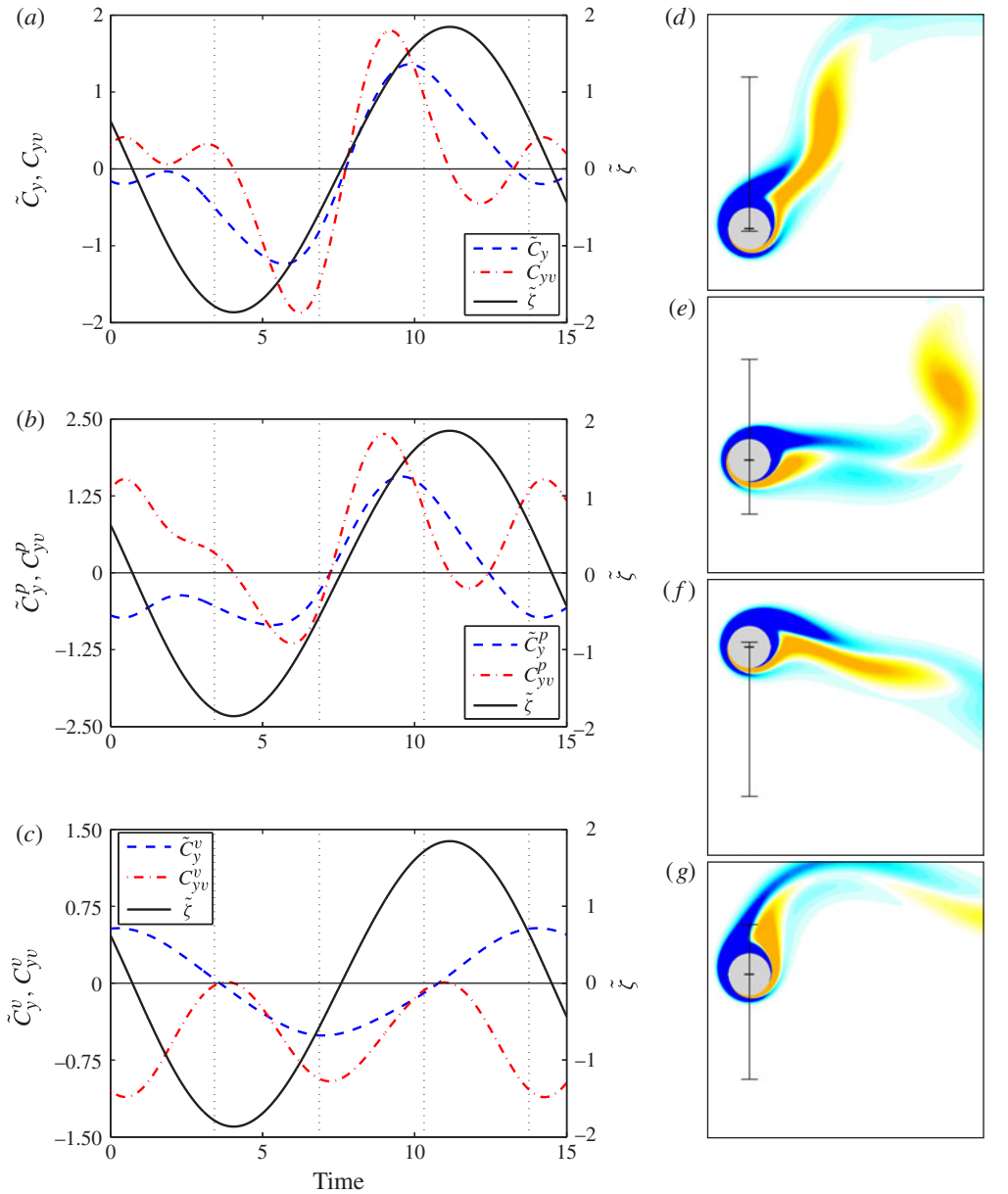

FIGURE 14. (Colour online) Same as figure 13, but now for $(\alpha, U^{\star}) = (3.5, 13)$ – T + S pattern. In panels (*d–g*), the isocontours of vorticity are in the range $\omega_z = \pm 1$.

13–15, panels (*a–c*), respectively; left axis) are plotted over one period of the cylinder oscillation. The fluctuation of the cylinder displacement is also plotted in these figures (right axis). In figures 13–15, panels (*d–g*), visualizations of the near-wake region through isocontours of vorticity are presented at four time instants indicated by black dotted lines in panels (*a–c*).

In the three cases, it can be observed that the unsteady wake pattern and the cylinder oscillation are synchronized, i.e. the lock-in condition is established. The

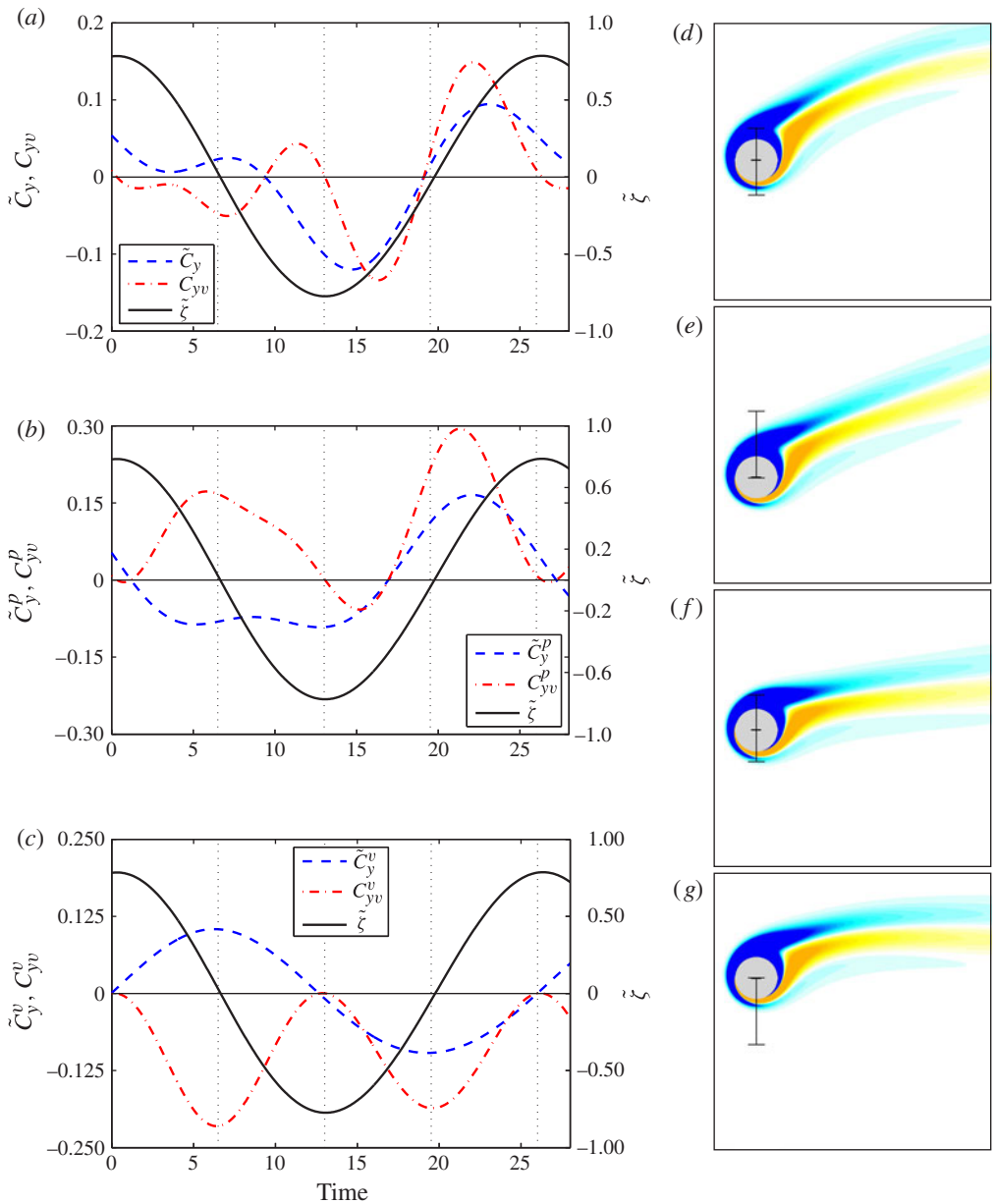

FIGURE 15. (Colour online) Same as figure 13, but now for $(\alpha, U^\star) = (3, 25)$ – U pattern. In panels (*d*–*g*), the isocontours of vorticity are in the range $\omega_z = \pm 1$.

magnitudes of the cross-flow force and its pressure and viscous parts exhibit strong variations from one configuration to another. However, some features persist for the three cases. In all cases, the body displacement is close to sinusoidal, which is not the case for the force coefficient; this is related to the occurrence of large higher harmonics, as will be discussed in § 5.2. As expected in the presence of forced rotation, which causes an asymmetry of the flow, the symmetry of $\tilde{C}_y$ over each half-cycle of oscillation is broken. The asymmetry is mainly due to the pressure

part of the force, whereas the viscous part remains relatively symmetrical. A joint monitoring of the time series and flow snapshots allows one to relate some events in the evolution of $\tilde{C}_y^p$ to the wake unsteadiness. For instance, the formation of a negative-vorticity vortex in figure 13(*e*) coincides with a positive peak of $\tilde{C}_y^p$ (figure 13*b*), i.e. the vortex seems to 'pull' the cylinder upwards. Conversely, the formation of a positive-vorticity vortex in figure 13(*d*,*g*) seems to 'pull' the cylinder downwards and may be connected with a negative peak of $\tilde{C}_y^p$. However, it should be recalled that vortex shedding is not required to observe fluctuations in the fluid force and associated structural vibrations, as illustrated in figure 15 (U wake pattern). Among the three selected configurations, differences may be noted in the phasing between the body response and the fluid force, as for instance for $\tilde{C}_y^p$ (figures 13*b* and 14*b*). The force–displacement phasing mechanisms are addressed in § 5.3.

The instantaneous energy transfer between the flow and the structure is quantified by means of the fluid force coefficient in phase with the cylinder velocity. As previously mentioned, the time-averaged component of the cross-flow force induced by the rotation (Magnus effect) causes a deflection of the cylinder time-averaged position (figure 5). Here, attention is paid to the body oscillations about their time-averaged position and thus to the energy transfer associated with the fluctuations of the force and its pressure and viscous parts. The corresponding coefficients are defined as follows:

$$C_{yv} = \frac{\sqrt{2}\tilde{C}_y\dot{\zeta}}{\sqrt{\overline{\dot{\zeta}^2}}}, \quad C_{yv}^p = \frac{\sqrt{2}\tilde{C}_y^p\dot{\zeta}}{\sqrt{\overline{\dot{\zeta}^2}}}, \quad C_{yv}^v = \frac{\sqrt{2}\tilde{C}_y^v\dot{\zeta}}{\sqrt{\overline{\dot{\zeta}^2}}}. \tag{5.1}$$

Positive values of these coefficients indicate that the flow excites the structural vibrations; negative values indicate that the vibrations are damped by the flow. Time series of C_{yv}, C_{yv}^p and C_{yv}^v are plotted in figures 13–15(*a*–*c*) (left axis). For self-sustained periodic oscillations, such as those generally observed in the present work, the time-averaged net energy transfer is zero ($\overline{C}_{yv} = 0$). Some observations, which are verified over the entire vibration region, can be made on the basis of the selected time series. The viscous part of the force principally damps the cylinder oscillations ($\overline{C}_{yv}^v < 0$), except in short time intervals where C_{yv}^v may become slightly positive, as shown in figure 13(*b*). The excitation of the body by the flow is mainly driven by the pressure part of the force ($\overline{C}_{yv}^p > 0$). Across the vibration region, the shape of the energy transfer over one cycle of oscillation exhibits substantial variations, which relate to the force frequency content and phasing; these aspects are investigated in the following subsections.

5.2. *Statistics and spectral analysis*

The time-averaged in-line and cross-flow force coefficients are plotted as functions of the reduced velocity in figure 16. For each rotation rate, the values of $\overline{C}_x$ and $\overline{C}_y$ in the rigidly mounted cylinder case are indicated by dashed lines. At a given reduced velocity, the time-averaged force coefficients globally decrease as α increases. The decrease of $\overline{C}_y$ results in an increasing downward deviation of the cylinder time-averaged position, as reported in § 3. Significant modulations of $\overline{C}_x$ and $\overline{C}_y$ are noted when the cylinder vibrates.

In the in-line direction, the body oscillations are accompanied by an amplification of $\overline{C}_x$ (figure 16*a*), as also noted in previous studies concerning non-rotating cylinders (Khalak & Williamson 1999; Carberry *et al.* 2005; Bourguet, Karniadakis &

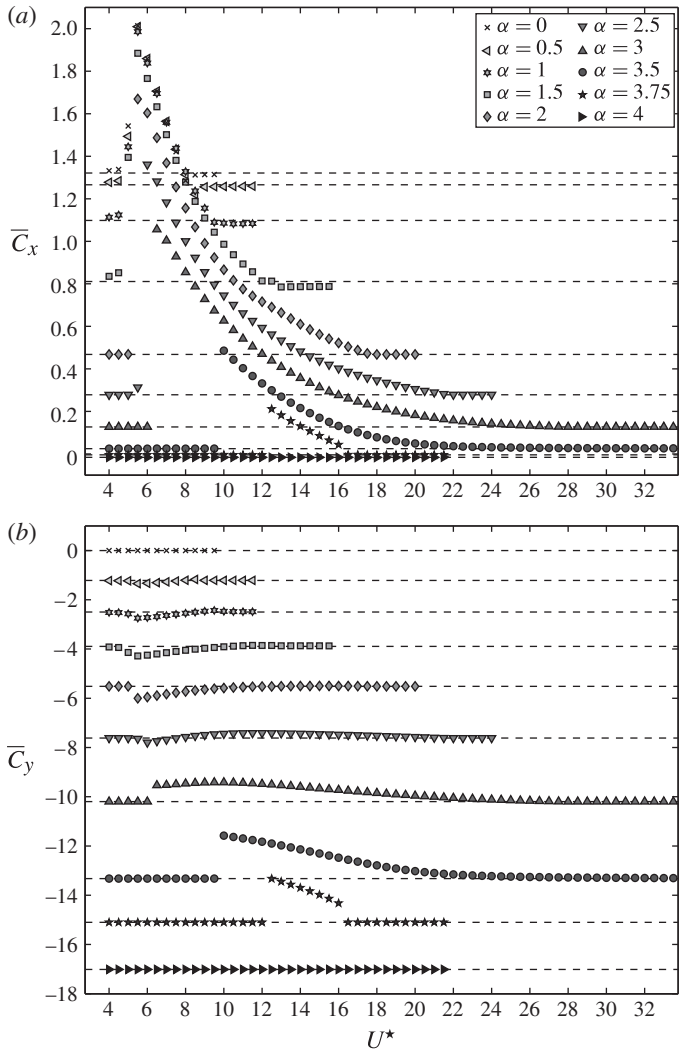

FIGURE 16. Time-averaged (*a*) in-line and (*b*) cross-flow force coefficients as functions of the reduced velocity. The dashed line indicates, for each rotation rate, the time-averaged force coefficient in the rigidly mounted cylinder case.

Triantafyllou 2011*b*). Regardless of the value of the rotation rate, $\overline{C}_x$ appears to follow a similar trend within the vibration region: for each α, the largest amplification occurs at the lowest reduced velocity, and then $\overline{C}_x$ decreases regularly across the vibration window. This trend was previously observed for non-rotating cylinders (e.g. Khalak & Williamson 1999) and the present results show that it persists in the rotating cylinder case. In addition, this behaviour seems to be independent of the wake pattern, as it is observed across the entire vibration region.

In the cross-flow direction, both positive and negative deviations of $\overline{C}_y$ from the rigidly mounted body value may occur when the rotating cylinder oscillates (figure 16*b*). Comparison with the map of the wake patterns (figure 8) suggests a possible link between the sign of the deviation and the type of flow topology. To

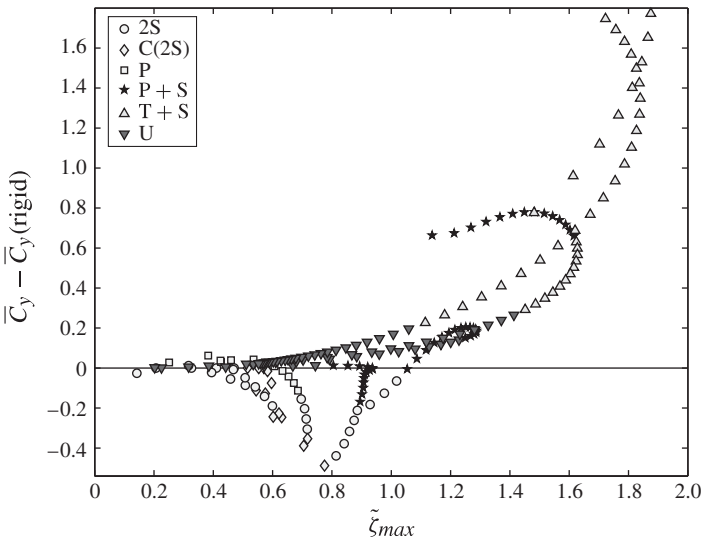

FIGURE 17. Deviation of the time-averaged cross-flow force coefficient from the value in the rigidly mounted cylinder case as a function of the maximum amplitude of vibration. The symbols represent the wake pattern.

clarify this aspect, the deviation of $\overline{C}_y$ is plotted in figure 17 as a function of the maximum vibration amplitude for all the points located within the vibration region, and the corresponding wake pattern is indicated by a symbol. As a general trend, it appears that the 2S pattern and its variations (P and C(2S)) are principally associated with negative deviations of $\overline{C}_y$, whereas the other patterns (P + S, T + S and U) are mainly related to positive deviations. A second trend can be identified: in the range of positive deviations, the deviation magnitude appears to increase globally with the amplitude of vibration; such behaviour is not observed for negative deviations.

Previous work has shown that the amplitudes of fluctuation of the fluid forces applied on a non-rotating cylinder tend to increase with the amplitude of vibration (Bishop & Hassan 1964; Khalak & Williamson 1999). A comparable trend is observed in the rotating cylinder case, as illustrated in figure 18, where the r.m.s. value of the in-line force coefficient fluctuation ($\tilde{C}_x$) is plotted as a function of the maximum vibration amplitude. Some modulations are, however, noted, since the largest r.m.s. value of $\tilde{C}_x$ for a given rotation rate does not necessarily coincide with the largest vibration amplitude. Similar observations can be made for the cross-flow force coefficient.

The r.m.s. values of the fluctuations of the cross-flow force coefficient and of its pressure and viscous parts are plotted as functions of the reduced velocity in figure 19, for all the studied rotation rates at which free vibrations develop, i.e. $\alpha \leqslant 3.75$. For each α, large variations of the r.m.s. values are noted within the vibration region. The r.m.s. value of $\tilde{C}_y$ exhibits a peak near the low-$U^\star$ limit of the vibration window and then decreases until the high-$U^\star$ limit of the vibration window; such behaviour was previously identified in the non-rotating cylinder case (Khalak & Williamson 1999; Govardhan & Williamson 2000) and the imposed rotation has no significant impact on the overall trend. The pressure part closely follows the evolution of the total force, while the viscous part presents a smoother behaviour and generally lower r.m.s. values.

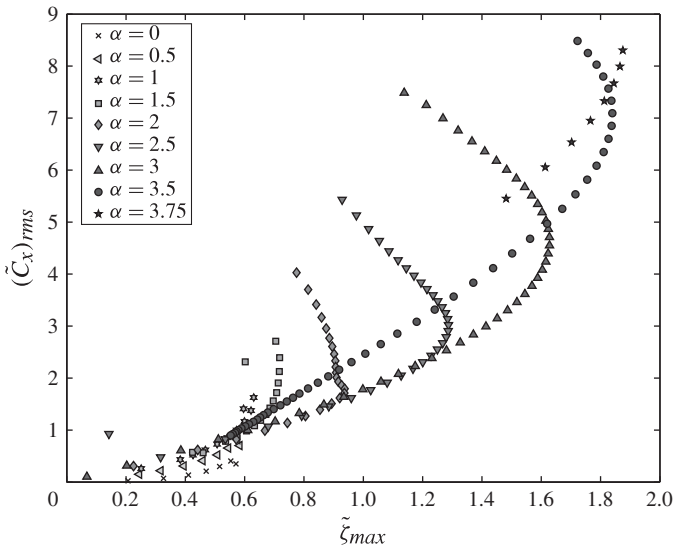

FIGURE 18. The r.m.s. value of the in-line force coefficient fluctuation as a function of the maximum amplitude of vibration.

The phasing of the cross-flow force and its pressure and viscous parts with the body displacement is examined in § 5.3.

A spectral analysis is performed in the following in order to shed light on some fluid–structure interaction mechanisms and to emphasize the impact of the imposed rotation on the force frequency content. In figures 20 and 21, the power spectral densities (PSDs) of the in-line and cross-flow force coefficients are plotted, for each rotation rate, as functions of the reduced velocity. The PSDs are normalized by the magnitude of the largest peak. At each reduced velocity, the predominant frequency of the wake is indicated by a triangle; this frequency is based on the PSD of time series of the cross-flow component of the flow velocity at a point located $10D$ downstream of the cylinder. The vortex shedding frequency in the rigidly mounted cylinder case is denoted by a dashed line ($\alpha < 1.8$). Within the vibration region, the body oscillation frequency is indicated by a circle.

The cylinder vibration frequency and the wake frequency generally coincide. The synchronization between the cylinder oscillation and the flow unsteadiness was illustrated in selected configurations in figures 13–15. The spectral analysis confirms that the flow-induced vibrations of the rotating cylinder occur under the lock-in condition, like VIV. However, as previously mentioned, the excitation of the rotating cylinder by the unsteady flow does not necessarily involve vortex shedding; indeed, large-amplitude oscillations are also noted when the wake exhibits the U pattern. The present *flow-induced vibrations under wake–body synchronization* differ from the galloping responses reported by Stansby & Rainey (2001) and Yogeswaran & Mittal (2011) for a rotating cylinder free to oscillate in both the in-line and cross-flow directions, since the galloping vibrations are not synchronized with the wake.

Within the vibration region, the fluid forces only peak at the vibration frequency or at frequencies corresponding to higher harmonics of the vibration frequency; therefore, the fluid forces are synchronized with the structural response. This contrasts with the above-mentioned galloping responses, where a high-frequency fluctuation of the forces,

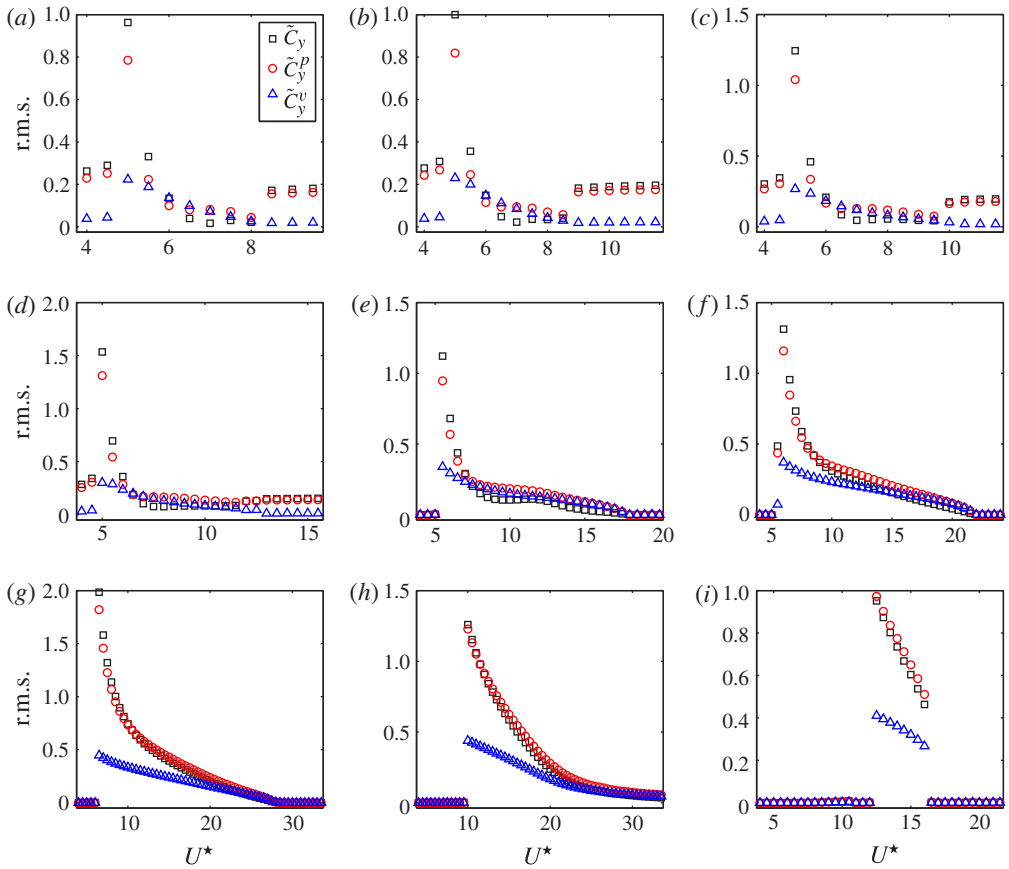

FIGURE 19. (Colour online) The r.m.s. values of the total ($\tilde{C}_y$), pressure ($\tilde{C}_y^p$) and viscous ($\tilde{C}_y^v$) cross-flow force coefficient fluctuations as functions of the reduced velocity for (*a*) $\alpha = 0$, (*b*) $\alpha = 0.5$, (*c*) $\alpha = 1$, (*d*) $\alpha = 1.5$, (*e*) $\alpha = 2$, (*f*) $\alpha = 2.5$, (*g*) $\alpha = 3$, (*h*) $\alpha = 3.5$ and (*i*) $\alpha = 3.75$.

due to vortex shedding, is superimposed onto the low-frequency component caused by body oscillation. The observed decreasing trend of the force frequencies within the vibration region thus corresponds to the decrease of the vibration frequency, which is driven by the decrease of the natural frequency as $U^\star$ increases. It is recalled that $U^\star = 1/f_n$ and that the vibration frequency differs but remains relatively close to f_n (figure 7*b*).

In the absence of rotation, the anti-symmetric nature of the vortex shedding pattern results in a ratio of 2 between the fundamental frequencies of the in-line and cross-flow forces. As previously noted in the rigidly mounted cylinder case (Mittal & Kumar 2003), the symmetry breaking induced by the imposed rotation results in a switch to a frequency ratio of 1, i.e. the fundamental frequencies of C_x and C_y are the same. This phenomenon is also observed in the present case, outside the vibration region, as shown in figures 20 and 21. A slight second harmonic contribution may persist in the C_x spectrum for $\alpha > 0$ (figure 20*b*) but it tends to vanish as α increases. The impact of the imposed rotation on the force spectra within the vibration region is addressed in this subsection.

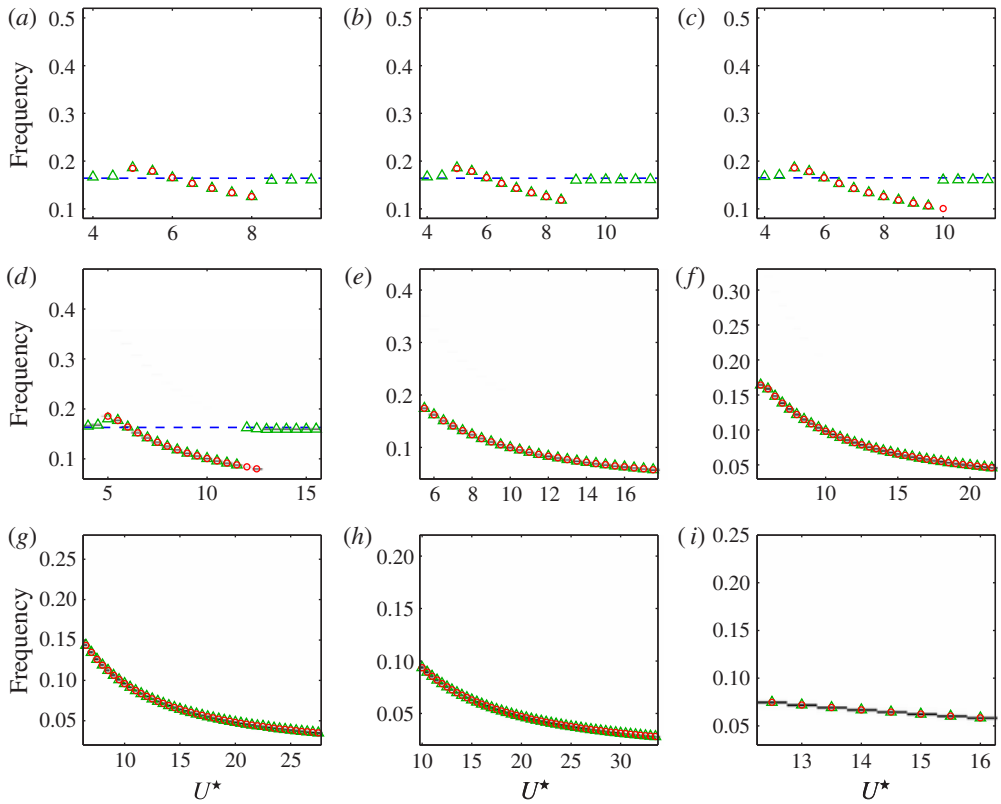

FIGURE 20. (Colour online) PSD of the in-line force coefficient (C_x) as a function of the reduced velocity for (*a*) $\alpha = 0$, (*b*) $\alpha = 0.5$, (*c*) $\alpha = 1$, (*d*) $\alpha = 1.5$, (*e*) $\alpha = 2$, (*f*) $\alpha = 2.5$, (*g*) $\alpha = 3$, (*h*) $\alpha = 3.5$ and (*i*) $\alpha = 3.75$. For each reduced velocity, the PSD is normalized by the magnitude of the largest peak. The greyscale levels range from 0 (white) to 1 (black). The cylinder vibration frequency is indicated by a circle and the predominant frequency of the wake by a triangle. In panels (*a*–*d*) ($\alpha < 1.8$), the dashed line denotes the vortex shedding frequency in the rigidly mounted cylinder case.

A striking feature of the force spectral content is the presence of large higher harmonics in the cross-flow direction. For instance, substantial contributions of the third harmonic can be noted in the C_y spectrum at $\alpha = 0$ (figure 21*a*), while both the second and third harmonics exhibit significant peaks at $\alpha = 1.5$ (figure 21*d*). In the non-rotating case, previous studies concerning flexible and flexibly mounted rigid cylinders have emphasized the existence of such higher harmonics and particularly the possible occurrence of a large third harmonic component in the cross-flow force spectrum (Jauvtis & Williamson 2004; Dahl *et al.* 2007; Vandiver, Jaiswal & Jhingran 2009; Dahl *et al.* 2010). Modarres-Sadeghi *et al.* (2010) have highlighted the influence of the force higher harmonics on the fatigue life of long marine risers. Wang, So & Chan (2003) and Wu, Ge & Hong (2012) proposed a simple model to relate the occurrence of the force higher harmonics to the body displacement, for a non-rotating cylinder subjected to a sinusoidal motion. Here, this model is extended to take into account the symmetry breaking caused by the imposed rotation.

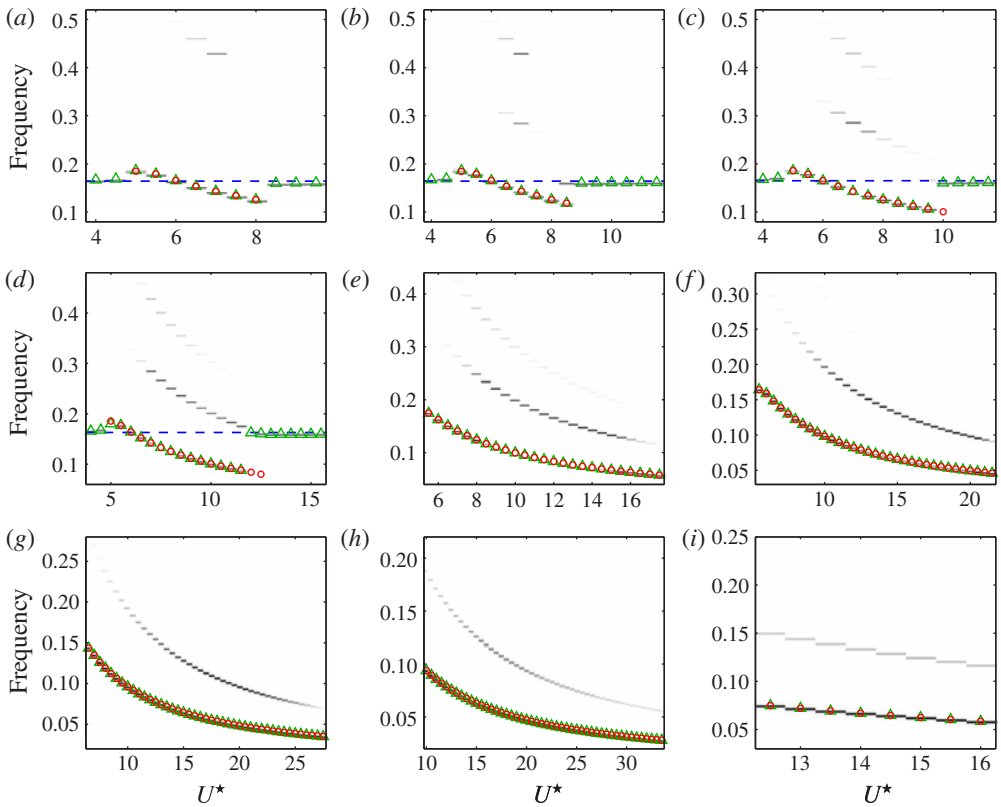

FIGURE 21. (Colour online) Same as figure 20 for the cross-flow force coefficient (C_y) at the same values of α.

Assuming a periodic structural response of fundamental frequency f, the cylinder displacement can be expanded as

$$\zeta = \sum_{n=0}^{\infty} \zeta_n \sin(2\pi nft + \phi_n), \tag{5.2}$$

where ζ_n and ϕ_n denote the spectral amplitude and phase lag associated with the nth harmonic. Owing to the vibration, the instantaneous velocity vector of the cylinder is not aligned with the x axis. The angle between the x axis and the axis parallel to the instantaneous velocity vector is $\theta = \arctan(-\dot{\zeta})$. The force coefficient parallel to the instantaneous velocity vector is referred to as C_d and the perpendicular force coefficient as C_l. The force coefficients in the stationary frame can be expressed as follows:

$$C_x = C_d \cos(\theta) - C_l \sin(\theta), \tag{5.3a}$$

$$C_y = C_d \sin(\theta) + C_l \cos(\theta). \tag{5.3b}$$

To simplify the analysis, θ is assumed to be small, which leads to

$$C_x = C_d + C_l \dot{\zeta}, \tag{5.4a}$$

$$C_y = -C_d \dot{\zeta} + C_l. \tag{5.4b}$$

The force coefficients expressed in the frame aligned with the instantaneous velocity vector are assumed to have a form analogous to the rigidly mounted cylinder case in the unsteady flow regime:

$$C_d = \overline{C}_d + C_{d1}\sin(2\pi ft + \phi_{d1}) + C_{d2}\sin(4\pi ft + \phi_{d2}), \tag{5.5a}$$

$$C_l = \overline{C}_l + C_{l1}\sin(2\pi ft + \phi_{l1}). \tag{5.5b}$$

Here $\overline{C}_d$ and $\overline{C}_l$ are the time-averaged values of C_d and C_l; C_{d1}, C_{l1} and C_{d2} are the first and second harmonic amplitudes; and ϕ_{d1}, ϕ_{l1} and ϕ_{d2} are the associated phase lags. The first harmonic of C_d and the time-averaged value of C_l are introduced to take into account the symmetry breaking caused by the rotation; in the absence of rotation, $\overline{C}_l = C_{d1} = 0$. The in-line and cross-flow force coefficients can be expressed as follows:

$$\begin{aligned} C_x = C_d + \pi f \sum_{n=1}^{\infty} n\zeta_n \{ & 2\overline{C}_l \cos(2\pi nft + \phi_n) + C_{l1}\sin[2\pi(n+1)ft + \phi_{l1} + \phi_n] \\ & - C_{l1}\sin[2\pi(n-1)ft - \phi_{l1} + \phi_n]\}, \end{aligned} \tag{5.6}$$

$$\begin{aligned} C_y = C_l - \pi f \sum_{n=1}^{\infty} n\zeta_n \{ & 2\overline{C}_d \cos(2\pi nft + \phi_n) + C_{d1}\sin[2\pi(n+1)ft + \phi_{d1} + \phi_n] \\ & - C_{d1}\sin[2\pi(n-1)ft - \phi_{d1} + \phi_n] + C_{d2}\sin[2\pi(n+2)ft + \phi_{d2} + \phi_n] \\ & - C_{d2}\sin[2\pi(n-2)ft - \phi_{d2} + \phi_n]\}. \end{aligned} \tag{5.7}$$

Therefore, several higher harmonic components may arise in the C_x and C_y spectra, depending among other things on the spectral content of the structural response. As previously mentioned, the cylinder oscillations remain close to sinusoidal. In the case of pure sinusoidal vibrations, i.e. $\zeta_n = 0$ for $n > 1$, the force coefficients become (without loss of generality ϕ_1 is set equal to 0°):

$$\begin{aligned} C_x = \overline{C}_d + \pi f\zeta_1 C_{l1}\sin(\phi_{l1}) + C_{d1}\sin(2\pi ft + \phi_{d1}) + 2\pi f\zeta_1\overline{C}_l\cos(2\pi ft) \\ + C_{d2}\sin(4\pi ft + \phi_{d2}) + \pi f\zeta_1 C_{l1}\sin(4\pi ft + \phi_{l1}), \end{aligned} \tag{5.8}$$

$$\begin{aligned} C_y = \overline{C}_l - \pi f\zeta_1 C_{d1}\sin(\phi_{d1}) + C_{l1}\sin(2\pi ft + \phi_{l1}) - 2\pi f\zeta_1\overline{C}_d\cos(2\pi ft) \\ - \pi f\zeta_1 C_{d2}\sin(2\pi ft + \phi_{d2}) - \pi f\zeta_1 C_{d1}\sin(4\pi ft + \phi_{d1}) \\ - \pi f\zeta_1 C_{d2}\sin(6\pi ft + \phi_{d2}). \end{aligned} \tag{5.9}$$

In the absence of rotation ($\overline{C}_l = C_{d1} = 0$), the above simple model indicates that, owing to the body oscillation, a third harmonic contribution may appear in the C_y spectrum, while the C_x spectrum is dominated by a single frequency equal to twice the cross-flow fundamental frequency. Under forced rotation ($\overline{C}_l \neq 0$ and $C_{d1} \neq 0$), the model suggests that both second and third harmonic contributions may arise in the C_y spectrum. The magnitude of the second harmonic of the in-line force in the rigidly mounted cylinder case (C_{d2}) decreases as α increases: therefore, the contribution of the third harmonic in the C_y spectrum is expected to decrease as α increases. Owing to the large magnitude of the time-averaged cross-flow force in the rigidly mounted cylinder case ($\overline{C}_l$), the first harmonic is expected to dominate the C_x spectrum, especially at high rotation rates. The trends predicted by the model are confirmed by the simulation results presented in figures 20 and 21. It is recalled that the above model, which is an extension of the model proposed by Wang *et al.* (2003), relies on several assumptions.

It is used in the present study only to illustrate the possible effect of the combined oscillation and rotation of the cylinder on the force frequency content.

The principal results of the spectral analysis can be summarized as follows. The flow-induced vibrations of the rotating cylinder occur under wake–body synchronization and, within the vibration region, the fluid forces are synchronized with the wake–body oscillation. The symmetry breaking caused by the rotation results in a switch of the ratio between the in-line and cross-flow force fundamental frequencies, from 2 for $\alpha = 0$ to 1 for $\alpha > 0$. Both within and outside the vibration region, the in-line force spectrum is dominated by the first harmonic contribution. In the absence of vibration, the cross-flow force spectrum presents a single first harmonic component. In contrast, large higher harmonic components appear in the cross-flow force spectrum when the cylinder vibrates: for $\alpha = 0$, as also noted in previous works, a significant third harmonic contribution may be observed; for $\alpha > 0$, both second and third harmonic components arise and the third harmonic contribution decreases with increasing rotation rate.

For a given rotation rate, the contributions of each harmonic component to the overall cross-flow force significantly vary across the vibration region. In particular, the first harmonic contribution seems to vanish for some values of the reduced velocity, for instance near $(\alpha, U^\star) = (1, 7)$ or $(2, 12)$, as shown in figure 21. This phenomenon is related to the mechanism of phasing between the force and the body displacement, as discussed in the following subsection.

5.3. *Phasing between force and displacement*

The phasing between the fluid forcing and the body response has been thoroughly studied in the literature related to cylinder VIV (Bearman 1984; Khalak & Williamson 1999; Carberry *et al.* 2001; Williamson & Govardhan 2004; Leontini *et al.* 2006; Dahl *et al.* 2010). The force–displacement phasing of the freely vibrating cylinder under forced rotation is investigated in this subsection. To present the typical phasing mechanism, periodic structural response and cross-flow force coefficient of fundamental frequency f are considered. The structural response is defined as in (5.2) and the force coefficient is expanded in a similar way as

$$C_y = \sum_{n=0}^{\infty} C_{yn} \sin(2\pi nft + \phi_{yn}), \tag{5.10}$$

where C_{yn} and ϕ_{yn} designate the spectral amplitude and phase lag associated with the nth harmonic. Since the body oscillation is generally close to sinusoidal, particular attention is paid to the phasing between the first harmonic components of the displacement and the force. Without loss of generality, ϕ_1 is selected equal to 0°, so that the phase difference between the first harmonics is equal to ϕ_{y1}. If ζ and C_y verify the dynamics equation (2.1), in which the structural damping is set to zero ($\xi = 0$), then (for $f \neq f_n$)

$$\phi_{y1} = 0^\circ \text{ or } 180^\circ \tag{5.11}$$

and

$$4\pi^2 f_n^2 (1 - f^{\star 2})\zeta_1 = \frac{C_{y1}}{2m} \cos(\phi_{y1}), \tag{5.12}$$

where, as previously defined, $f^\star = f/f_n$. As a result, the system may exhibit two possible phasing states: (i) the first harmonics of the force and displacement are

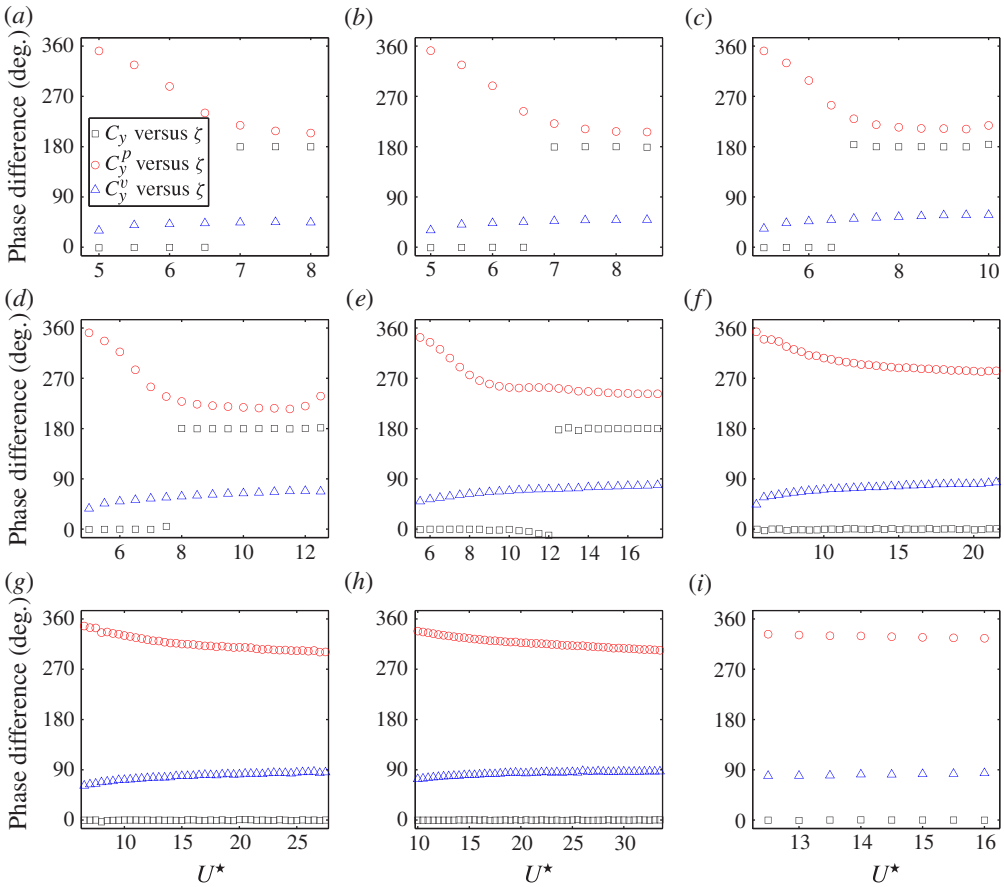

FIGURE 22. (Colour online) Phase differences between the total (C_y), pressure (C_y^p) and viscous (C_y^v) cross-flow force coefficients and the cylinder displacement as functions of the reduced velocity for (*a*) $\alpha = 0$, (*b*) $\alpha = 0.5$, (*c*) $\alpha = 1$, (*d*) $\alpha = 1.5$, (*e*) $\alpha = 2$, (*f*) $\alpha = 2.5$, (*g*) $\alpha = 3$, (*h*) $\alpha = 3.5$ and (*i*) $\alpha = 3.75$.

in phase ($\phi_{y1} = 0°$) and the vibration frequency is lower than the natural frequency in vacuum ($f^\star < 1$); (ii) the first harmonics of the force and displacement are in antiphase ($\phi_{y1} = 180°$) and the vibration frequency is larger than the natural frequency in vacuum ($f^\star > 1$). A phase jump occurs when the vibration frequency passes through the value of the natural frequency; for $f^\star = 1$, the contribution of the first harmonic of the force (C_{y1}) vanishes since $C_{y1}\cos(\phi_{y1}) = C_{y1}\sin(\phi_{y1}) = 0$. Previous work concerning VIV of non-rotating cylinders has emphasized the existence of the two above phasing states, over the lock-in range. It should be mentioned that (5.11) and (5.12) hold in both the non-rotating and rotating cylinder cases.

In order to clarify the impact of the cylinder rotation on the force–displacement phasing mechanism, the phase difference between the first harmonics of ζ and $C_y(\phi_{y1})$ is plotted as a function of the reduced velocity in figure 22, for each rotation rate (squares). For $\alpha \leqslant 2$, both phasing states ($\phi_{y1} = 0°$ and $180°$) are observed within the vibration window, whereas the force and displacement remain in phase at higher rotation rates, regardless of the value of $U^\star$. Comparison with the evolution of the vibration frequency (figure 7*b*) confirms that the phase jump coincides rigorously

with $f^\star = 1$, i.e. the cylinder vibrates at the natural frequency. As reported in § 3, the vibration frequency exhibits a global decrease as the rotation rate increases; this explains why the phase jump tends to drift towards higher values of the reduced velocity as α increases. For $\alpha \geqslant 2.5$ cases, the vibration frequency is always lower than the natural frequency: in these cases, no phase jump occurs and only the type (i) phasing state is observed.

As expected on the basis of the above analysis, low magnitudes of the first harmonic component can be noted near the phase jumps in figure 21. In these regions, the contributions of the higher harmonic components become predominant, as for instance near $U^\star = 7$ at $\alpha = 1$.

As also noted in previous studies concerning non-rotating cylinders (e.g. Govardhan & Williamson 2000), the phase jump does not coincide with a switch of the wake pattern. In order to shed some light on the physical nature of the phase discontinuity, the phase differences between the first harmonic of ζ and the first harmonics of the pressure (C_y^p) and viscous (C_y^v) parts of C_y are also plotted in figure 22 as circles and triangles, respectively. Contrary to the total cross-flow force, the phase differences associated with C_y^p and C_y^v, referred to as ϕ_{y1}^p and ϕ_{y1}^v, respectively, vary continuously as functions of $U^\star$. Hence, the phase jump of C_y is not due to a jump in the phase of its pressure or viscous parts; instead, it results from the combination of two force components whose phases vary smoothly across the vibration window. The phase difference associated with the viscous part remains in a narrow range of phase difference angles, between 30 and 90° approximately; a slight overall increase may be noted as a function of α, while for each rotation rate, ϕ_{y1}^v tends to increase with $U^\star$. The phase difference associated with the pressure part exhibits larger variations, especially in the range of low reduced velocities. As indicated in § 5.1, some events in the evolution of the pressure part of C_y can be connected to the formation of vortices in the wake. Therefore, it is expected that the phasing of vortex formation will influence the phasing of C_y^p. However, it can be observed that ϕ_{y1}^p may still vary in the absence of vortex shedding, as for instance for $U^\star > 22$ at $\alpha = 3.5$, where the wake is characterized by the U pattern.

The fact that no phase jump of the cross-flow force occurs at high rotation rate was related to the global decrease of the vibration frequency as α increases. In the following, this trend of the structural response frequency is investigated in light of the variability of the effective added mass.

5.4. *Effective added mass*

Previous studies concerning cylinder VIV have shown that the effective added mass coefficient induced by the fluid force in phase with the body acceleration may substantially depart from the potential flow value of 1 (Sarpkaya 1979; Vikestad, Vandiver & Larsen 2000; Dahl *et al.* 2010; Bourguet, Karniadakis & Triantafyllou 2011*a*). The effective added mass coefficient can be defined as follows:

$$C_m = -\frac{2}{\pi}\frac{\overline{C_y\ddot{\zeta}}}{\overline{\ddot{\zeta}^2}}. \tag{5.13}$$

For periodic displacement (5.2) and force coefficient (5.10), an effective added mass coefficient, involving the response first harmonic component only, may be defined by removing all the higher harmonic contributions in (5.13) (Dahl *et al.* 2010):

$$C_m^1 = \frac{C_{y1}\cos(\phi_{y1})}{2\pi^3 f^2 \zeta_1}. \tag{5.14}$$

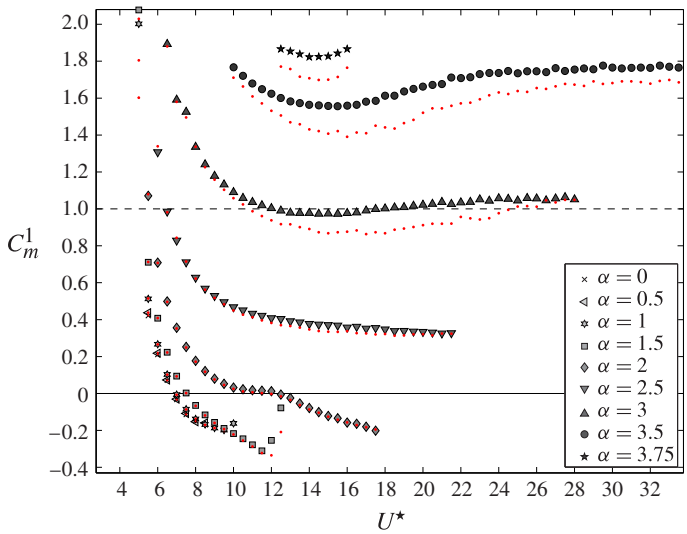

FIGURE 23. (Colour online) Effective added mass coefficient associated with the response first harmonic component (C_m^1 defined in (5.14)) as a function of the reduced velocity. The effective added mass coefficient based on the total response (C_m defined in (5.13)) is indicated by a dot (red online) for each pair $(\alpha, U^\star)$.

In the case of sinusoidal responses, C_m^1 is equal to C_m. The coefficient C_m^1 is significant as it relates directly to the vibration frequency as follows (Williamson & Govardhan 2004):

$$f^\star = \sqrt{\frac{m}{m + \frac{1}{4}\pi C_m^1}}. \tag{5.15}$$

For each rotation rate, C_m^1 is plotted as a function of the reduced velocity in figure 23. The values of C_m are also presented, for comparison purposes (dots; red online).

Slight differences may be noted between C_m and C_m^1, especially at high rotation rates, due to the occurrence of small higher harmonic components in the response. However, as previously mentioned, the higher harmonic contributions are limited and the response remains close to sinusoidal in all cases, which explains the global similarity between C_m and C_m^1 evolutions. The effective added mass coefficient generally differs from 1. The decreasing trend observed as a function of the reduced velocity in the non-rotating cylinder case was also reported in previous studies (e.g. Dahl *et al.* 2010). The global increase of the effective added mass coefficient as α increases is associated with the previously mentioned decrease of the vibration frequency. For $\alpha \geqslant 2.5$ cases, the vibration frequency remains lower than the natural frequency (figure 7*b*) and the cross-flow force phase jump vanishes (figure 22). This phenomenon is related to the strictly positive value of the effective added mass over the entire vibration window.

So far, the analysis of the coupled fluid–structure system has been carried out on the basis of two-dimensional simulations of the flow. The three-dimensional transition in the flow at high rotation rates and its possible influence on the interaction mechanisms are investigated in the next section.

6. Three-dimensional transition

Previous studies concerning rigidly mounted rotating cylinders have shown that rotation substantially alters the flow three-dimensional transition scenario compared to the non-rotating case (Mittal 2004; El Akoury *et al.* 2008; Meena *et al.* 2011; Rao *et al.* 2013*b*). At $Re = 100$, the recent linear stability analyses reported by Pralits *et al.* (2013) and Rao *et al.* (2013*a*) predict that the flow should become three-dimensional for $\alpha \approx 3.7$. The occurrence of the three-dimensional transition under the effect of forced rotation is examined in the following on the basis of three-dimensional direct numerical simulation results. The objective here is not to provide an extensive analysis of the transition mechanisms; instead, this section aims at clarifying the potential impact of the three-dimensional transition on the fluid–structure interaction phenomena previously described under the two-dimensional flow assumption. The case of a rigidly mounted cylinder is considered as a first step in § 6.1 in order to identify the region of transition and quantify its influence on the fluid forces. The flexibly mounted cylinder case is addressed in § 6.2.

6.1. *Rigidly mounted cylinder*

The flow past a rigidly mounted cylinder subjected to forced rotation is visualized in figure 24 by means of instantaneous isosurfaces of the spanwise and streamwise vorticity components, for three values of the rotation rate, $\alpha \in \{3.5, 3.75, 4.0\}$. The flow is steady in this range of rotation rates, as also noted in the two-dimensional simulations. The present three-dimensional simulations show that the flow remains two-dimensional at $\alpha = 3.5$. In contrast, an undulation of the spanwise vorticity layers is observed at $\alpha = 3.75$ and tends to amplify at $\alpha = 4.0$; this undulation is accompanied by the development of elongated vortical structures in the streamwise direction. As a result, the flow past a rigidly mounted rotating cylinder at $Re = 100$ becomes three-dimensional at a critical rotation rate located between 3.5 and 3.75; this observation is in agreement with the predictions based on linear stability analyses (Pralits *et al.* 2013; Rao *et al.* 2013*a*). The three-dimensional flow pattern is comparable to those reported by Mittal (2004) and Meena *et al.* (2011) at $Re = 200$. The spanwise wavelength of the three-dimensional pattern is approximately equal to $1.7D$; the above-mentioned linear stability analyses predict a similar wavelength.

In order to quantify the impact of the three-dimensional transition on the fluid forces, the evolutions of C_x and C_y are plotted along the cylinder span in figure 25, for $\alpha = 3.75$ and $\alpha = 4.0$. It is recalled that the flow, though three-dimensional, remains steady for both rotation rates, thus $C_x = \overline{C}_x$ and $C_y = \overline{C}_y$. Spanwise fluctuations of the force coefficients can be noted in both directions, with an amplification of the fluctuations as α increases; this amplification correlates to the previously mentioned increasing spanwise undulation of the flow. The span-averaged values of the force coefficients are indicated in figure 25 by dashed lines while the values issued from two-dimensional simulations are denoted by dash-dotted lines. In the range of rotation rates considered in the present work ($\alpha \leqslant 4.0$), it appears that the three-dimensional transition in the flow has only a very limited influence on the span-averaged fluid forces.

Two steady flow patterns, the D^+ and D^- patterns, have been identified outside of the vibration region, on the basis of two-dimensional simulations in § 4. The present three-dimensional simulations allow one to refine the description of these patterns. The limit between the D^+ and D^- flow patterns was defined based on a change in the sign of the in-line force. As can be noted in figure 25(*a*), the passage from positive to negative values of span-averaged C_x occurs in the range $\alpha \in [3.5, 3.75]$ (as in

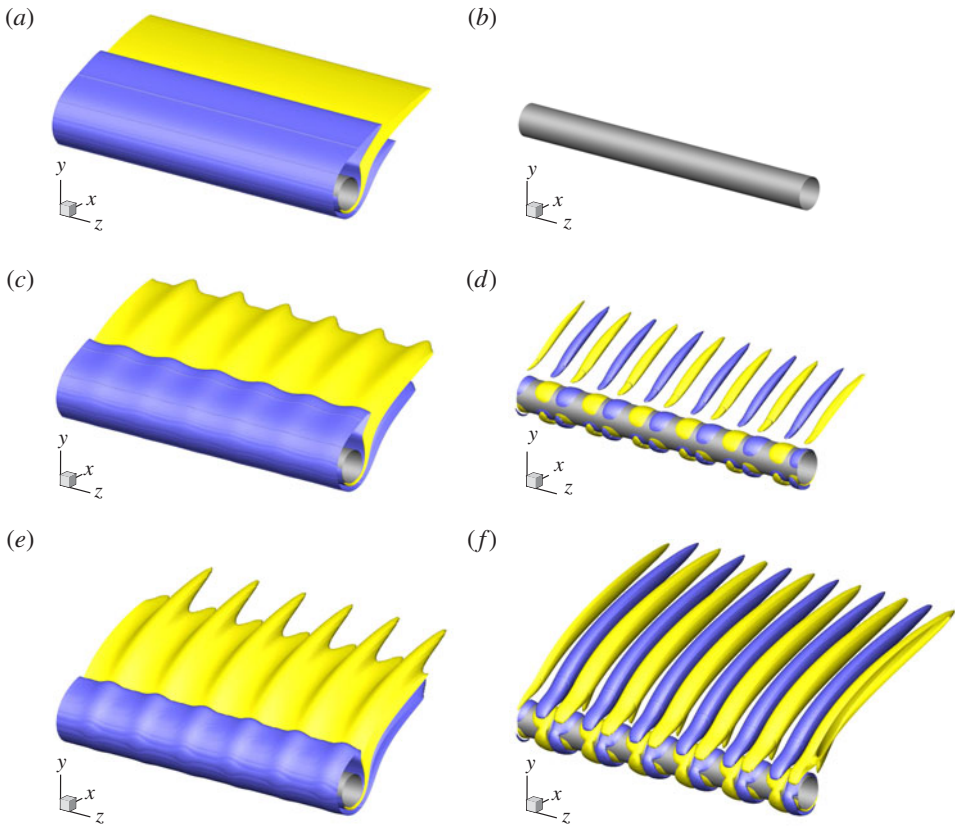

FIGURE 24. (Colour online) Instantaneous isosurfaces of (*a*,*c*,*e*) spanwise ($\omega_z = \pm 0.2$) and (*b*,*d*,*f*) streamwise ($\omega_x = \pm 0.2$) vorticity in the rigidly mounted cylinder case, for (*a*,*b*) $\alpha = 3.5$, (*c*,*d*) $\alpha = 3.75$ and (*e*, *f*) $\alpha = 4.0$. Part of the computational domain is shown.

the two-dimensional case), which is also the range associated with the onset of the three-dimensional transition. As a result, the D^+ pattern is essentially two-dimensional, whereas the D^- pattern is characterized by an undulation of the flow along the span, in addition to the inversion of the spanwise vorticity layers reported in § 4 and also visible in figure 24(*c*,*e*).

The three-dimensional transition occurs in a range of rotation rates that corresponds to the upper limit of the vibration region determined in § 3, on the basis of two-dimensional simulations. This is also the area where the largest vibration amplitudes have been observed. As a consequence, the effect of the three-dimensional transition on the behaviour of the coupled fluid–structure system needs to be clarified in order to ensure the validity of the previous analysis in this region of the parameter space.

6.2. *Flexibly mounted cylinder*

To assess the impact of the three-dimensional transition in the flexibly mounted cylinder case, two points have been selected in the parameter space, in the range of rotation rates where the transition occurs for a rigidly mounted cylinder.

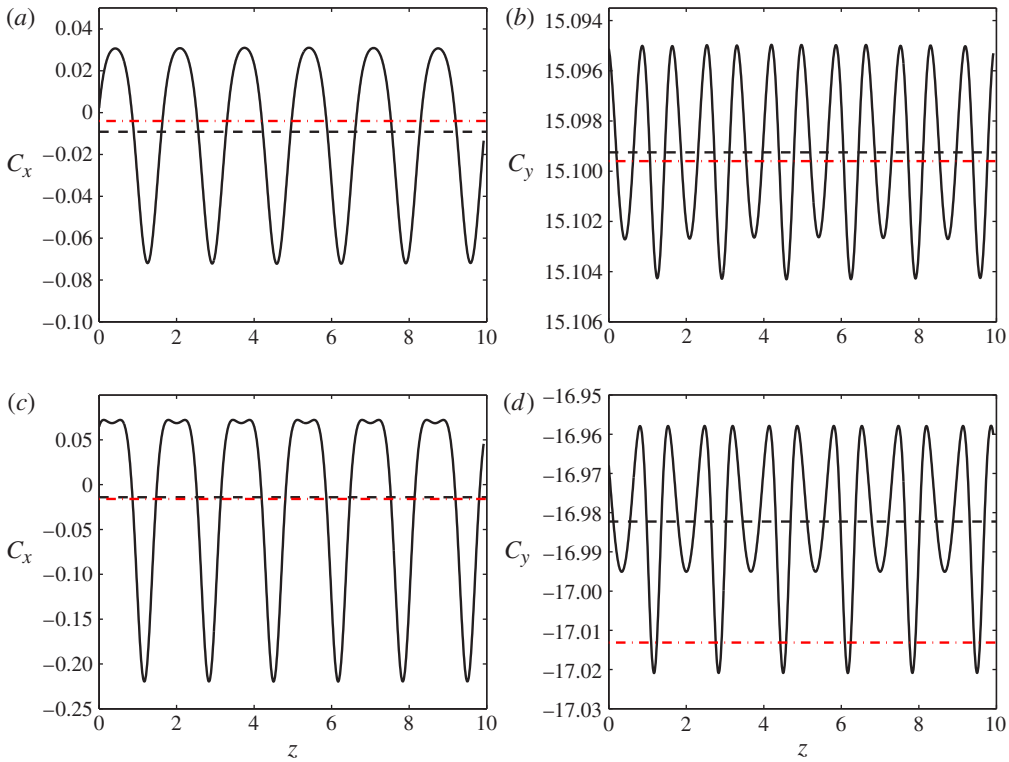

FIGURE 25. (Colour online) Spanwise evolution of the (*a*,*c*) in-line and (*b*,*d*) cross-flow force coefficients in the rigidly mounted cylinder case, for (*a*,*b*) $\alpha = 3.75$ and (*c*,*d*) $\alpha = 4.0$. The span-averaged value of the force coefficient is indicated by a dashed line, while the value issued from two-dimensional simulation is represented by a dash-dotted line.

The first point, $(\alpha, U^\star) = (3.75, 13)$, is located within the vibration region identified in § 3, in the area of maximum amplitudes of oscillation (figure 7*a*). A visualization of the flow through instantaneous isosurfaces of spanwise vorticity issued from the three-dimensional simulation is presented in figure 26. Contrary to the rigidly mounted cylinder case at the same rotation rate (figure 24*c*), it appears that the flow is strictly two-dimensional. The behaviour of the fluid–structure system, including the vibration amplitude and frequency, the wake pattern and the fluid forces, is identical to that issued from the two-dimensional simulation. Previous studies concerning non-rotating cylinders have shown that the onset of three-dimensionality may be delayed when the cylinder oscillates transversely (e.g. Berger 1967; Leontini, Thompson & Hourigan 2007); a similar phenomenon is observed in the present case of a rotating cylinder. Owing to the large amplitudes of the cylinder oscillations in the upper part of the vibration region, a comparable delay of the three-dimensional transition is likely to occur across the entire vibration window.

The second point, $(\alpha, U^\star) = (4, 14)$, is chosen outside the vibration region defined on the basis of two-dimensional simulations. In this case, as also noted from the two-dimensional results in § 3, no vibration of the cylinder develops and the flow remains steady. The flow pattern is identical to that observed in the rigidly mounted cylinder case (figure 24*e*,*f*). Compared to the two-dimensional case, the equilibrium position of

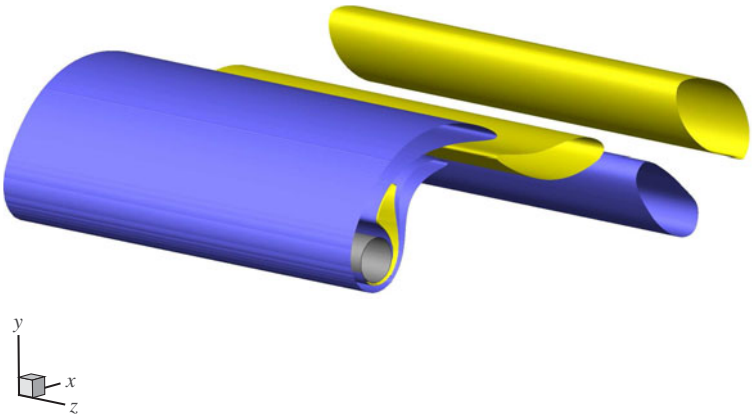

FIGURE 26. (Colour online) Instantaneous isosurfaces of spanwise vorticity ($\omega_z = \pm 0.2$) for $(\alpha, U^\star) = (3.75, 13)$. Part of the computational domain is shown.

the cylinder is slightly displaced upwards due to the modification of the span-averaged value of C_y, equal to -16.98 in the three-dimensional case versus -17.01 under the two-dimensional flow assumption.

Therefore, the three-dimensional simulation results reported in this section corroborate the previous two-dimensional analysis.

7. Conclusions

The transverse flow-induced vibrations of a circular cylinder subjected to forced rotation have been investigated by means of numerical simulations, at a Reynolds number equal to 100. The impact of the symmetry breaking due to the imposed rotation on the phenomenon of vortex-induced vibrations, previously studied in the absence of rotation, has been analysed over a wide range of reduced velocities and rotation rates. The analysis was essentially based on two-dimensional simulations. Three-dimensional simulations were performed in selected points of the parameter space in order to confirm the two-dimensional results and examine the potential influence of the flow three-dimensional transition, which occurs at high rotation rates, for $\alpha \in [3.5, 3.75]$, when the cylinder is rigidly mounted. The principal findings of this work can be summarized as follows.

Large-amplitude vibrations through wake–body synchronization. The cylinder is found to exhibit free oscillations from $\alpha = 0$ up to a rotation rate close to 4. As a result, vibrations occur for $\alpha < 1.8$ but also for $\alpha \geqslant 1.8$, i.e. in a range of rotation rates where the rotation cancels the vortex shedding in the rigidly mounted cylinder case. Under forced rotation, the vibrations may reach amplitudes close to 1.9 cylinder diameters, thus three times larger than the maximum vibration amplitude observed for a non-rotating cylinder. For all rotation rates, the bell-shaped evolution of the vibration amplitude as a function of the reduced velocity is comparable to that noted for non-rotating cylinder VIV, although the vibration window may widen substantially. Over the entire vibration region identified in the $(\alpha, U^\star)$ parameter space, the structural response and the wake unsteadiness appear to be synchronized. The free vibrations of the rotating cylinder thus occur under a condition of wake–body synchronization similar to the lock-in condition driving non-rotating cylinder VIV.

This behaviour contrasts with the galloping-like responses, which do not involve the lock-in condition and exhibit amplitudes that increase unboundedly with $U^\star$.

Novel wake patterns under forced rotation. Several flow patterns including novel wake topologies have been observed across the parameter space. In the absence of vibration, the 2S pattern dominates for $\alpha < 1.8$, while steady patterns characterized by elongated layers of spanwise vorticity occur at higher rotation rates. Two steady patterns have been identified: the D^+ pattern (for $\alpha < 3.7$ approximately), where the negative-vorticity layer is located above the positive one, which results in a positive in-line force; and the D^- pattern (for $\alpha > 3.7$ approximately), which is characterized by an inversion of the vorticity layers and $C_x < 0$. Owing to the three-dimensional transition, the vorticity layers of the D^- pattern exhibit a spanwise undulation of wavelength approximately equal to 1.7 cylinder diameters. Within the vibration region, the 2S pattern and its variations (C(2S) and P) dominate the low-rotation-rate area, which corresponds to structural responses of moderate amplitudes and high to moderate frequencies. Three wake patterns occur in the high-rotation-rate zone of the vibration region. The P + S pattern and a novel asymmetric pattern composed of a triplet of vortices and a single vortex shed per cycle, referred to as T + S, are associated with large-amplitude vibrations at moderate to low frequencies. The T + S pattern dominates the region of maximum-amplitude vibrations, which includes the range of high rotation rates where the flow three-dimensional transition occurs in the rigidly mounted cylinder case. Three-dimensional simulation results in this region indicate that the flow around the vibrating cylinder remains two-dimensional. In the low-frequency range, the flow exhibits a transverse undulation of the spanwise vorticity layers, without vortex shedding. This new wake topology is referred to as the U pattern. Therefore, it is found that free oscillations of the rotating cylinder may occur in the absence of vortex detachment. Consequently, the terminology *flow-induced vibrations under wake–body synchronization* is preferred to 'vortex-induced vibrations' in order to designate the present structural responses.

Impact of rotation on force frequency content and phasing mechanism. Large modulations of the fluid forces, including a substantial amplification of $\overline{C}_x$, are noted when the cylinder vibrates. The type of wake pattern is found to relate to the deviation of $\overline{C}_y$ from the value observed in the rigidly mounted case due to the Magnus effect: the 2S, C(2S) and P patterns are associated with negative deviations, while positive deviations are observed under the P + S, T + S and U patterns. As also noted in previous works, in the absence of rotation, the transverse oscillation of the cylinder results in a large third harmonic component in the cross-flow force, while the in-line force is dominated by a single frequency equal to twice the cross-flow fundamental frequency. The symmetry breaking caused by the rotation directly impacts the frequency content of the fluid forces: the ratio between the in-line and cross-flow force fundamental frequencies switches from 2 to 1, the in-line force spectrum is dominated by the first harmonic component, while both second and third harmonic contributions arise in the cross-flow force spectrum. The imposed rotation also influences the phasing between the cross-flow force and the structural response: the 180° phase jump occurring when the vibration frequency crosses the oscillator natural frequency tends to drift towards higher reduced velocities as α increases and disappears at high rotation rates. This phenomenon is associated with an alteration of the vibration frequency, which is found to globally decrease when the rotation rate increases, in relation with the strong variability of the effective added mass coefficient.

Acknowledgement

This work was performed using HPC resources from CALMIP (grant 2013-P1248).

REFERENCES

BADR, H. M., COUTANCEAU, M., DENNIS, S. C. R. & MÉNARD, C. 1990 Unsteady flow past a rotating circular cylinder at Reynolds numbers 10^3 and 10^4. *J. Fluid Mech.* **220**, 459–484.

BEARMAN, P. W. 1984 Vortex shedding from oscillating bluff bodies. *Annu. Rev. Fluid Mech.* **16**, 195–222.

BEARMAN, P. W. 2011 Circular cylinder wakes and vortex-induced vibrations. *J. Fluids Struct.* **27**, 648–658.

BEARMAN, P. W., GARTSHORE, I. S., MAULL, D. J. & PARKINSON, G. V. 1987 Experiments on flow-induced vibration of a square-section cylinder. *J. Fluids Struct.* **1**, 19–34.

BERGER, E. 1967 Suppression of vortex shedding and turbulence behind oscillating cylinders. *Phys. Fluids* **10**, S191.

BISHOP, R. E. D. & HASSAN, A. Y. 1964 The lift and drag forces on a circular cylinder oscillating in a flowing fluid. *Proc. R. Soc.* A **277**, 51–75.

BLACKBURN, H. M. & HENDERSON, R. D. 1999 A study of two-dimensional flow past an oscillating cylinder. *J. Fluid Mech.* **385**, 255–286.

BLEVINS, R. D. 1990 *Flow-Induced Vibration*. Van Nostrand Reinhold.

BOURGUET, R., KARNIADAKIS, G. E. & TRIANTAFYLLOU, M. S. 2011*a* Lock-in of the vortex-induced vibrations of a long tensioned beam in shear flow. *J. Fluids Struct.* **27**, 838–847.

BOURGUET, R., KARNIADAKIS, G. E. & TRIANTAFYLLOU, M. S. 2011*b* Vortex-induced vibrations of a long flexible cylinder in shear flow. *J. Fluid Mech.* **677**, 342–382.

BRAZA, M., CHASSAING, P. & HA MINH, H. 1986 Numerical study and physical analysis of the pressure and velocity fields in the near wake of a circular cylinder. *J. Fluid Mech.* **165**, 79–130.

BRIKA, D. & LANEVILLE, A. 1993 Vortex-induced vibrations of a long flexible circular cylinder. *J. Fluid Mech.* **250**, 481–508.

CARBERRY, J., SHERIDAN, J. & ROCKWELL, D. 2001 Forces and wake modes of an oscillating cylinder. *J. Fluids Struct.* **15**, 523–532.

CARBERRY, J., SHERIDAN, J. & ROCKWELL, D. 2005 Controlled oscillations of a cylinder: forces and wake modes. *J. Fluid Mech.* **538**, 31–69.

CHEW, Y. T., CHENG, M. & LUO, S. C. 1995 A numerical study of flow past a rotating circular cylinder using a hybrid vortex scheme. *J. Fluid Mech.* **299**, 35–71.

CORLESS, R. M. & PARKINSON, G. V. 1988 A model of the combined effects of vortex-induced oscillation and galloping. *J. Fluids Struct.* **2**, 203–220.

COUTANCEAU, M. & MÉNARD, C. 1985 Influence of rotation on the near-wake development behind an impulsively started circular cylinder. *J. Fluid Mech.* **158**, 399–446.

DAHL, J. M., HOVER, F. S., TRIANTAFYLLOU, M. S., DONG, S. & KARNIADAKIS, G. E. 2007 Resonant vibrations of bluff bodies cause multivortex shedding and high frequency forces. *Phys. Rev. Lett.* **99**, 144503.

DAHL, J. M., HOVER, F. S., TRIANTAFYLLOU, M. S. & OAKLEY, O. H. 2010 Dual resonance in vortex-induced vibrations at subcritical and supercritical Reynolds numbers. *J. Fluid Mech.* **643**, 395–424.

EL AKOURY, R., BRAZA, M., PERRIN, R., HARRAN, G. & HOARAU, Y. 2008 The three-dimensional transition in the flow around a rotating cylinder. *J. Fluid Mech.* **607**, 1–11.

EVANGELINOS, C. & KARNIADAKIS, G. E. 1999 Dynamics and flow structures in the turbulent wake of rigid and flexible cylinders subject to vortex-induced vibrations. *J. Fluid Mech.* **400**, 91–124.

GOVARDHAN, R. & WILLIAMSON, C. H. K. 2000 Modes of vortex formation and frequency response of a freely vibrating cylinder. *J. Fluid Mech.* **420**, 85–130.

HOVER, F. S., TECHET, A. H. & TRIANTAFYLLOU, M. S. 1998 Forces on oscillating uniform and tapered cylinders in crossflow. *J. Fluid Mech.* **363**, 97–114.

JAUVTIS, N. & WILLIAMSON, C. H. K. 2004 The effect of two degrees of freedom on vortex-induced vibration at low mass and damping. *J. Fluid Mech.* **509**, 23–62.

JEON, D. & GHARIB, M. 2001 On circular cylinders undergoing two-degree-of-freedom forced motions. *J. Fluids Struct.* **15**, 533–541.

KANG, S., CHOI, H. & LEE, S. 1999 Laminar flow past a rotating circular cylinder. *Phys. Fluids* **11**, 3312–3321.

KARNIADAKIS, G. E. & SHERWIN, S. 1999 *Spectral/hp Element Methods for CFD*. 1st edn. Oxford University Press.

KHALAK, A. & WILLIAMSON, C. H. K. 1999 Motions, forces and mode transitions in vortex-induced vibrations at low mass-damping. *J. Fluids Struct.* **13**, 813–851.

KIM, J., KIM, D. & CHOI, H. 2001 An immersed-boundary finite-volume method for simulations of flow in complex geometries. *J. Comput. Phys.* **171**, 132–150.

KLAMO, J. T., LEONARD, A. & ROSHKO, A. 2006 The effects of damping on the amplitude and frequency response of a freely vibrating cylinder in cross-flow. *J. Fluids Struct.* **22**, 845–856.

LEONTINI, J. S., STEWART, B. E., THOMPSON, M. C. & HOURIGAN, K. 2006 Wake state and energy transitions of an oscillating cylinder at low Reynolds number. *Phys. Fluids* **18**, 067101.

LEONTINI, J. S., THOMPSON, M. C. & HOURIGAN, K. 2007 Three-dimensional transition in the wake of a transversely oscillating cylinder. *J. Fluid Mech.* **577**, 79–104.

LUCOR, D. & TRIANTAFYLLOU, M. S. 2008 Parametric study of a two degree-of-freedom cylinder subject to vortex-induced vibrations. *J. Fluids Struct.* **24**, 1284–1293.

MEENA, J., SIDARTH, G. S., KHAN, M. H. & MITTAL, S. 2011 Three-dimensional instabilities in flow past a spinning and translating cylinder. In *IUTAM Symposium on Bluff Body Flows, IIT-Kanpur, India* (ed. S. Mittal & G. Biswas), pp. 75–78.

MITTAL, S. 2004 A finite element study of incompressible flows past oscillating cylinders and aerofoils. *J. Appl. Mech.* **71**, 89–95.

MITTAL, S. & KUMAR, B. 2003 Flow past a rotating cylinder. *J. Fluid Mech.* **476**, 303–334.

MITTAL, S. & TEZDUYAR, T. E. 1992 A finite element study of incompressible flows past oscillating cylinders and aerofoils. *Intl J. Numer. Meth. Fluids* **15**, 1073–1118.

MODARRES-SADEGHI, Y., MUKUNDAN, H., DAHL, J. M., HOVER, F. S. & TRIANTAFYLLOU, M. S. 2010 The effect of higher harmonic forces on fatigue life of marine risers. *J. Sound Vib.* **329**, 43–55.

MODI, V. J. 1997 Moving surface boundary-layer control: a review. *J. Fluids Struct.* **11**, 627–663.

NAUDASCHER, E. & ROCKWELL, D. 1994 *Flow-Induced Vibrations: an Engineering Guide*. Dover.

NAVROSE, & MITTAL, S. 2013 Free vibrations of a cylinder: 3-D computations at $Re = 1000$. *J. Fluids Struct.* **41**, 109–118.

NEMES, A., ZHAO, J., LO JACONO, D. & SHERIDAN, J. 2012 The interaction between flow-induced vibration mechanisms of a square cylinder with varying angles of attack. *J. Fluid Mech.* **710**, 102–130.

NEWMAN, D. J. & KARNIADAKIS, G. E. 1997 A direct numerical simulation study of flow past a freely vibrating cable. *J. Fluid Mech.* **344**, 95–136.

PAÏDOUSSIS, M. P., PRICE, S. J. & DE LANGRE, E. 2010 *Fluid–Structure Interactions: Cross-Flow-Induced Instabilities*. Cambridge University Press.

PRALITS, J. O., BRANDT, L. & GIANNETTI, F. 2010 Instability and sensitivity of the flow around a rotating circular cylinder. *J. Fluid Mech.* **650**, 513–536.

PRALITS, J. O., GIANNETTI, F. & BRANDT, L. 2013 Three-dimensional instability of the flow around a rotating circular cylinder. *J. Fluid Mech.* **730**, 5–18.

PRANDTL, L. 1926 Application of the 'Magnus effect' to the wind propulsion of ships. *NACA Tech. Mem.* 367.

PRASANTH, T. K. & MITTAL, S. 2008 Vortex-induced vibrations of a circular cylinder at low Reynolds numbers. *J. Fluid Mech.* **594**, 463–491.

RAGHAVAN, K. & BERNITSAS, M. M. 2011 Experimental investigation of Reynolds number effect on vortex-induced vibration of rigid circular cylinder on elastic supports. *Ocean Engng* **38**, 719–731.

RAO, A., LEONTINI, J. S., THOMPSON, M. C. & HOURIGAN, K. 2013*a* Three-dimensionality in the wake of a rapidly rotating cylinder in uniform flow. *J. Fluid Mech.* **730**, 379–391.

RAO, A., LEONTINI, J. S., THOMPSON, M. C. & HOURIGAN, K. 2013*b* Three-dimensionality in the wake of a rotating cylinder in a uniform flow. *J. Fluid Mech.* **717**, 1–29.

SARPKAYA, T. 1979 Vortex-induced oscillations: a selective review. *Trans. ASME: J. Appl. Mech.* **46**, 241–258.

SARPKAYA, T. 2004 A critical review of the intrinsic nature of vortex-induced vibrations. *J. Fluids Struct.* **19**, 389–447.

SHEN, L., CHAN, E.-S. & LIN, P. 2009 Calculation of hydrodynamic forces acting on a submerged moving object using immersed boundary method. *Comput. Fluids* **38**, 691–702.

SHIELS, D., LEONARD, A. & ROSHKO, A. 2001 Flow-induced vibration of a circular cylinder at limiting structural parameters. *J. Fluids Struct.* **15**, 3–21.

SINGH, S. P. & MITTAL, S. 2005 Vortex-induced oscillations at low Reynolds numbers: hysteresis and vortex-shedding modes. *J. Fluids Struct.* **20**, 1085–1104.

STANSBY, P. K. & RAINEY, R. C. T. 2001 On the orbital response of a rotating cylinder in a current. *J. Fluid Mech.* **439**, 87–108.

STANSBY, P. K. & SLAOUTI, A. 1993 Simulation of vortex shedding including blockage by the random-vortex and other methods. *Intl J. Numer. Meth. Fluids* **17**, 1003–1013.

STOJKOVIĆ, D., BREUER, M. & DURST, F. 2002 Effect of high rotation rates on the laminar flow around a circular cylinder. *Phys. Fluids* **14**, 3160–3178.

STOJKOVIĆ, D., SCHÖN, P., BREUER, M. & DURST, F. 2003 On the new vortex shedding mode past a rotating circular cylinder. *Phys. Fluids* **15**, 1257–1260.

VANDIVER, J. K., JAISWAL, V. & JHINGRAN, V. 2009 Insights on vortex-induced, travelling waves on long risers. *J. Fluids Struct.* **25**, 641–653.

VIKESTAD, K., VANDIVER, J. K. & LARSEN, C. M. 2000 Added mass and oscillation frequency for a circular cylinder subjected to vortex-induced vibrations and external disturbance. *J. Fluids Struct.* **14**, 1071–1088.

WANG, X. Q., SO, R. M. C. & CHAN, K. T. 2003 A nonlinear fluid force model for vortex-induced vibration of an elastic cylinder. *J. Sound Vib.* **260**, 287–305.

WILLIAMSON, C. H. K. 1988 The existence of two stages in the transition to three-dimensionality of a cylinder wake. *Phys. Fluids* **31**, 3165–3168.

WILLIAMSON, C. H. K. & GOVARDHAN, R. 2004 Vortex-induced vibrations. *Annu. Rev. Fluid Mech.* **36**, 413–455.

WILLIAMSON, C. H. K. & ROSHKO, A. 1988 Vortex formation in the wake of an oscillating cylinder. *J. Fluids Struct.* **2**, 355–381.

WU, X., GE, F. & HONG, Y. 2012 A review of recent studies on vortex-induced vibrations of long slender cylinders. *J. Fluids Struct.* **28**, 292–308.

YOGESWARAN, V. & MITTAL, S. 2011 Vortex-induced and galloping response of a rotating circular cylinder. In *IUTAM Symposium on Bluff Body Flows, IIT-Kanpur, India* (ed. S. Mittal & G. Biswas), pp. 153–156.

ZHAO, M., CHENG, L. & ZHOU, T. 2013 Numerical simulation of vortex-induced vibration of a square cylinder at a low Reynolds number. *Phys. Fluids* **25**, 023603.

ZHOU, C. Y., SO, R. M. C. & LAM, K. 1999 Vortex-induced vibrations of an elastic circular cylinder. *J. Fluids Struct.* **13**, 165–189.